2010

Models of galaxy collisions in Stephan's Quintet and other interacting systems

Jeong-sun Hwang
Iowa State University

Models of galaxy collisions in Stephan's Quintet

and other interacting systems

by

Jeong-Sun Hwang

A dissertation submitted to the graduate faculty

in partial fulfillment of the requirements for the degree of

DOCTOR OF PHILOSOPHY

Major: Astrophysics

Program of Study Committee:
Curtis J. Struck, Major Professor
Lee Anne Willson
Charles Kerton
James P. Vary
William J. Gutowski Jr.

Iowa State University

Ames, Iowa

2010

TABLE OF CONTENTS

LIST OF TABLES

LIST OF FIGURES

ACKNOWLEDGEMENTS

First and foremost, I would like to thank my advisor, Dr. Curtis Struck, for everything he has done for me. His guidance, patience, and insights have helped me so much throughout my doctoral program. Thank you Curt, I couldn't ask for a better advisor. I am very grateful to all of my committee members, Dr. Lee Anne Willson, Dr. Charles Kerton, Dr. James P. Vary, and Dr. William Gutowski, for taking time out of their busy schedules for me and providing valuable suggestions on my thesis. A special thanks goes to Lee Anne who always showed generosity and encouraged me. I am also thankful to professors and my collaborators, Dr. Bert Crawley, Dr. David Johnston, Dr. Steve Kawaler, Dr. Martin Pohl, Dr. Phil Appleton, and Dr. Florent Renaud, for their help and kindness.

It is my pleasure to thank many faculty members, instructors, staff, and my colleagues in the Department of Physics & Astronomy at Iowa State University for their support and hospitality. It is hard for me to write all of their names, because I have met so many good people and friends here. However, I should at least mention my group member, Brad Peterson, office mates, Qian Wang, Bert Pablo, and Erik Johnson, and Kim Arvidsson and Tom Stroman. Thank you all for your support and friendship. I also wish to thank Keith and Candace Textor in Ames, and Cari and Brian Ewert in Minneapolis for their help and friendship.

Finally, I would like to express my heartfelt thanks to my parents, sisters, and my husband, Soo-hyeon Nam. Without their love and support I would not be where I am today. I love you all so much. I dedicate this dissertation to my parents, my husband, and Jehovah.

ABSTRACT

This dissertation describes numerical studies of three interacting galaxy systems. First, hydrodynamical models of the collisions in the famous compact galaxy group, Stephan's Quintet, were constructed to investigate the dynamical interaction history and evolution of the intergalactic gas. It has been found that with a sequence of two-at-a-time collisions, most of the major morphological and kinematical features of the group were well reproduced in the models. The models suggest the two long tails extending from NGC 7319 toward NGC 7320c may be formed simultaneously from a strong collisional encounter between the two galaxies, resulting in a thinner and denser inner tail than the outer one. The tails then also run parallel to each other as observed. The model results support the idea that the group-wide shock detected in multi-wavelength observations between NGC 7319 and 7318b and the starburst region north of NGC 7318b are triggered by the current high-speed collision between NGC 7318b and the intergalactic gas. It is expected that other compact groups containing rich extended features like Stephan's Quintet can be modeled in similar ways, and that sequences of two-at-a-time collisions will be the general rule.

The second set of hydrodynamical simulations were performed to model the peculiar galaxy pair, Arp 285. This system possesses a series of star-forming complexes in an unusual tail-like feature extending out perpendicular to the disk of the northern galaxy. Several conceptual ideas for the origin of the tail-like feature were examined. The models suggest that the bridge material falling into the gravitational potential of the northern disk overshoots the disk; as more bridge material streams into the region, compression drives star formation. This work on star-formation in the pile-up region can be extended to the studies of the formation of tidal dwarf galaxies or globular clusters.

Thirdly, the development of spiral waves was studied with numerical models of fast galaxy collisions involving a disk with a high value of the Toomre Q parameter. The models found that spirals slowly developed in the disk do not dissipate in a few outer disk orbital time. The waves in the models persist for a long time, more than 10 outer disk rotation periods, while winding ever tighter. Since fast collisions are common in many galaxy groups and cluster environments, the phenomena and effect presented in the work may be one of the several processes that contribute to galaxy harassment, and a contributor to the Butcher-Oemler effect.

CHAPTER 1. INTRODUCTION

Galaxies are not isolated, rather they interact with neighboring galaxies and are affected by the environment. Since the extent of galaxy halos is comparable to the separations between them, and dependent on environment, galaxy interactions (collisions) are common and play important role in galaxy evolution. Galaxy collisions and mergers can lead a variety of phenomena, including not only morphological changes but also enhanced star formations and active nuclei. Many aspects of galaxy interaction and evolution have been revealed by the two complementary means, observations and numerical simulations.

In the 1940's, the clustering tendency of galaxies was already clear from early observations. Holmberg thought the groups and clusters of galaxies might result from successive "tidal captures" between closely passing galaxies. To demonstrate the idea, he produced, for the first time, models of encounters between two galaxies using an analogue computer with light bulbs and photocells (Holmberg 1941); each galaxy was set up with 37 light bulbs representing stellar mass points and gravity at different distances was measured from the $1/r^2$ light intensities. Although the experiment (including the conceptual idea) was problematic, the models showed signatures on tidal disturbances by interactions.

Until the early 1970's, there was still much debate on the tidal deformation of interacting galaxies, particularly if very extended filamentary features observed in some galaxies could also be of tidal origins, or perhaps due to magnetic fields or strong explosions. This was answered by a seminal work in the field of galaxy collisions and evolution, performed by the brothers Toomre (Toomre & Toomre 1972). They constructed simple models of close (parabolic) encounters between two galaxies using a restricted three-body calculation; a companion galaxy in the models was represented as a central mass point and a main galaxy as a central mass point

with an initial disk surrounded by a few hundred massless test particles. The models were very simplified by modern standards (considering only the inverse-square force of gravity and ignoring anything else, for example self-gravity), however, they convincingly illustrated the formation of narrow elongated tidal features (so called tidal "bridges" and "tails") from the model disks (see Figure 1.1). They also reproduced the basic stellar morphologies of several specific binary systems which posses very extended peculiar features, showing that tidal forces alone in close encounters could deform the appearances of the systems as observed. Their model results and discussion on galaxy interactions and mergers revolutionized our understanding on the subject and brought the field to central research importance.

Following Toomre & Toomre (1972), various collisional features and dynamics of encounters were understood. For example, (collisional) ring galaxies were found to be produced by head-on collisions of a dense companion passing through a larger disk galaxy (see review of Appleton & Struck-Marcell 1996). Toomre (1978) showed with numerical models that as the impact point in a vertical collision is offset from the center of a victim disk to its edge, the resultant tidal features smoothly change from rings to spirals. Shell structure around elliptical galaxies would be formed by the accretion of small companion galaxy (e.g., Quinn 1984).

The recognition of extended massive dark halos surrounding galaxies (Ostriker & Peebles 1973) largely changed our view of galaxies and their interactions. It was noted that galaxy collisions and mergers would be much more common with such halos due to the increasing cross-sections (e.g. Toomre 1977). Several self-consistent numerical models of merging disk galaxies, which included rich interstellar medium and dark matter halos, (e.g. Mihos & Hernquist 1994, Elmegreen et al. 1993, Barnes & Hernquist 1996) showed that tidal forces during encounters can develop central bars out of disk material, ejection of gas out to tidal tails, and during the final stages of a collision massive gas flow into the cores of the merger remnants yielding strong starbursts.

The relation between interactions and star formation histories was first noted by Larson & Tinsley (1978). They found that the scatter in the broad band optical (UBV) colors of peculiar galaxies from Arp atlas was larger than that of normal-looking galaxies from the

Hubble atlas, suggesting bursts of star formations in the peculiar systems due to interactions. Further evidence of interaction-induced star formation was found at various wavelengths (e.g. Struck-Marcell & Tinsley 1978, Kennicutt et al. 1987); however some interactions do not cause the phenomena (e.g. Keel et al. 1985, Kennicutt et al. 1987). The ultra-luminous infrared galaxies (ULIRGs) observed from the IRAS all-sky survey nearly all show features of merging galaxies (e.g. Sanders et al. 1986); which is consistent with numerical simulations results indicating strong central starburst in merger remnants (e.g. Mihos & Hernquist 1994, Barnes & Hernquist 1996).

More recently, with improved observations and computer power, research on galaxy interactions and evolution has been growing rapidly, becoming wider and deeper. For example, the properties of high redshift galaxies have been studied extensively in the last decade. Theoretical calculations of galaxy merger rate have been attempted from different cosmological structure formation simulations. Consequently, statistical studies, such as the merger rate, cosmic star formation rate, and morphology as a function of redshift, have also been carried out. However, we still need to understand dynamics of nearby interactions in detail to create a full picture. For example, recently there have been intensive research on tidal dwarf galaxies and the nature of star cluster formation to better understand modes of star formation.

I have performed numerical modeling for various interacting galaxy systems, from binaries to compact groups, and investigated the evolution driven by interactions and the properties of the resultant large-scale features of the systems. I have studied the compact galaxy group, Stephan's Quintet, in depth by numerical hydrodynamical simulations. I present this work in the following Chapter 2. In Chapters 3 and 4, I describe another specific modeling work on the peculiar pair, Arp 285 system (NGC 2856/4), and the numerical study of spiral wave development by fast galaxy collisions, respectively. Finally, I summarize the primary results of each numerical study and discuss the implications and future work in Chapter 5

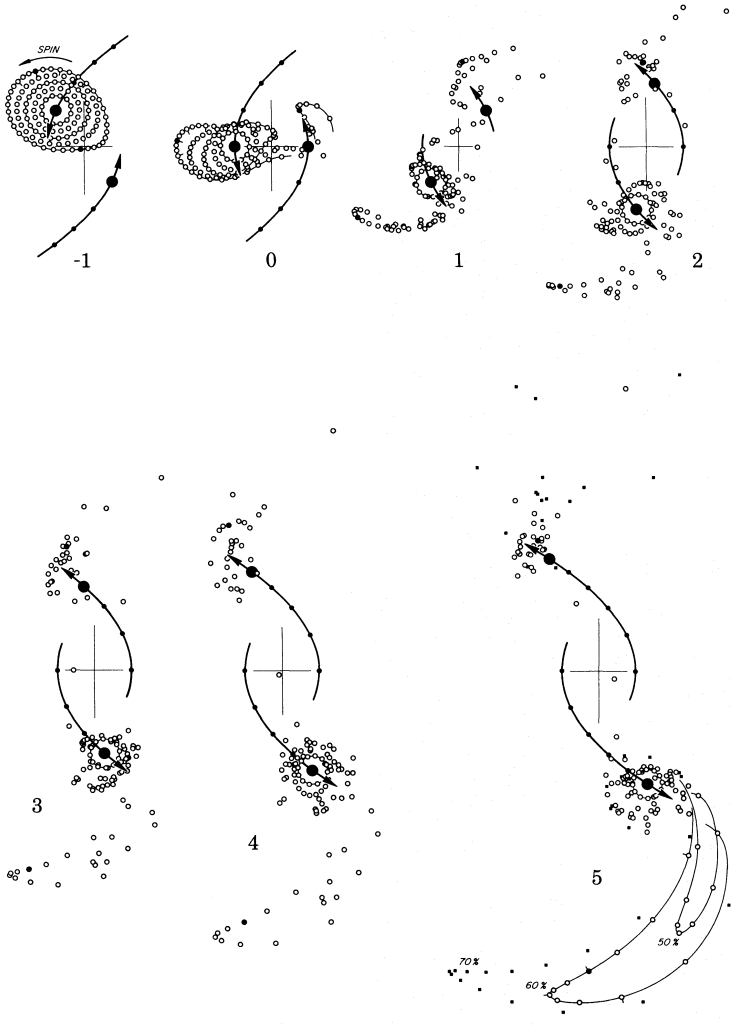

Figure 1.1 Development of tidal bridges and tails from a flat prograde parabolic passage of a companion of equal mass (Toomre & Toomre 1972). Time is measured from the perigalactic instant ($t = 0$) and the number shown in each snapshot indicates time in the unit of 10^8 years. The violent tearing away of the test particles is seen after the closest approach.

CHAPTER 2. MODELS OF STEPHAN'S QUINTET: HYDRODYNAMICAL CONSTRAINTS ON THE GROUP'S EVOLUTION

2.1 Introduction

In investigating the evolution of an interacting galaxy system, multi-wavelength observations and dynamical modeling are complementary. On the one hand, high-resolution observations in different wave bands reveal important physical quantities and information about various physical processes in the system. By interpreting these quantities and the possible causes of the processes, we can learn about the dynamical state and deduce the plausible interaction history of the system. On the other hand, well-constrained numerical models provide not only the direct testing of the plausible interactions but it also may yield additional constraints or information such as the halo profiles of the systems.

Ever since Toomre & Toomre (1972) successfully simulated the stellar morphologies of several interacting galaxy pairs, explaining the formation of their peculiar structures (which were quite mysterious at that time), and with help of growing computer technology, numerical simulations have become more popular and important means in studying interacting systems.

Compact groups (compact and relatively isolated systems of several galaxies) often show highly distorted features of interactions. Due to the dense environment, galaxy interactions would occur more frequently in more complex ways in compact groups than binary systems. These groups are thus important environments for studying various interaction and merger effects, and furthermore, overall galaxy evolution.

However, unlike binary systems where computer simulations have often been used to interpret observations, simulations for compact groups have not been frequently attempted,

especially to model specific groups. Constraining models is much more difficult or sometimes not possible if the system has experienced multiple strong interactions with multiple members and the structural or kinematical evidence of interactions has been largely erased.

For some compact groups, however, numerical modeling looks feasible. For example, if a system maintains characteristic tidal features or collisional ring structures then it is possible to limit the plausible interactions to a few cases. The presence of recent interaction is also helpful with the short duration and perhaps more strong, unique evidence of the "young" interaction. In addition, even though a group appears to have experienced multiple interactions, if each interaction involved mainly two galaxies rather than three or more members (i.e., a sequence of "two-at-a-time" interactions), then modeling interpretations could be more tractable, as in a binary system.

Stephans Quintet (hereafter SQ; also known as HCG 92, Arp 319, and VV 288; see Figure 2.1), one of the first compact galaxy groups identified (Hickson 1982), has many of these properties. It shows strongly disturbed structural and kinematical features, such as extended tidal tails, disturbed arms and ring-like features, and rich intergalactic medium (IGM) with little gas remaining in the central region of every member galaxy (see Figure 2.3). Moreover, the group is thought to be experiencing a high-speed collision between a member (NGC 7318b) and its IGM; multi-wavelength observations, including radio continuum (e.g., Allen & Hartsuiker 1972; Xu et al. 2003) and X-rays (e.g., Trinchieri et al. 2003, 2005; see Figure 2.2(a)), have consistently shown a huge elongated feature in the IGM which has been widely accepted as a shock front triggered by an ongoing or very recent collision.

More recently, Appleton et al. (2006) discovered strong almost pure-rotational H_2 line emission ($\sim$24 kpc long if at 94 Mpc) along the X-ray-emitting shock front. In follow-up observations (Cluver et al. 2010), the line emission at the main shock region was detected over $\sim$480 kpc^2 with a luminosity exceeding that of the X-rays from the shock. This surprising detection of warm molecular gas coexisting with hot gas in the shock region motivated me to study the hydrodynamics of the system. In addition, although many observational and theoretical research programs have helped to understand various features in SQ, the evolutionary

history and some aspects of the group remain unclear, so there is a need for further detailed simulations to understand the system.

Given all of those interesting features and observational constraints, I have performed smoothed particle hydrodynamics (SPH; see Appendix A for details) simulations of SQ, taking four strongly interacting members into account (Hwang et al. 2010). Previously, my collaborators started modeling of this system with a purely gravitational N-body code and examined interaction history and large-scale stellar morphology (Renaud et al. 2010). (Hereafter I distinguish the previous work (code, models, etc) with the term "N-body"; if not specified, the reference is to the current SPH code, models. etc). This study extends the N-body work adding thermohydrodynamical effects (especially for the shock); with new models, the origins of the large-scale features and the dynamical evolution of the intergalactic gas of the system are further investigated in this work.

In Section 2.2, I first briefly review the members and the large-scale features characterizing SQ and consider the plausible interaction history of the group and model constraints. Then I explain the simulation code and model details of this work in Section 2.3 and present the model results in Section 2.4. Finally, I summarize and discuss the main results and the ramifications in Section 2.5.

2.2 Overview of SQ properties and model constraints

2.2.1 The members and the large-scale features

The optical morphology of SQ is presented in Figure 2.1. By apparent proximity, SQ traditionally denotes the group of five galaxies, NGC 7317, NGC 7318a, NGC 7318b, NGC 7319, and NGC 7320. However, NGC 7320 is a foreground galaxy which has a considerably smaller redshift than others (Burbidge & Burbidge 1961) without any indications of interactions with the group. Actually, NGC 7320c, located far east of NGC 7319, is considered to be linked to the group, particularly to NGC 7319. As I conduct numerical modeling of SQ, I treat the five physically related galaxies, excluding NGC 7320 and adding NGC 7320c, as the members of the quintet.

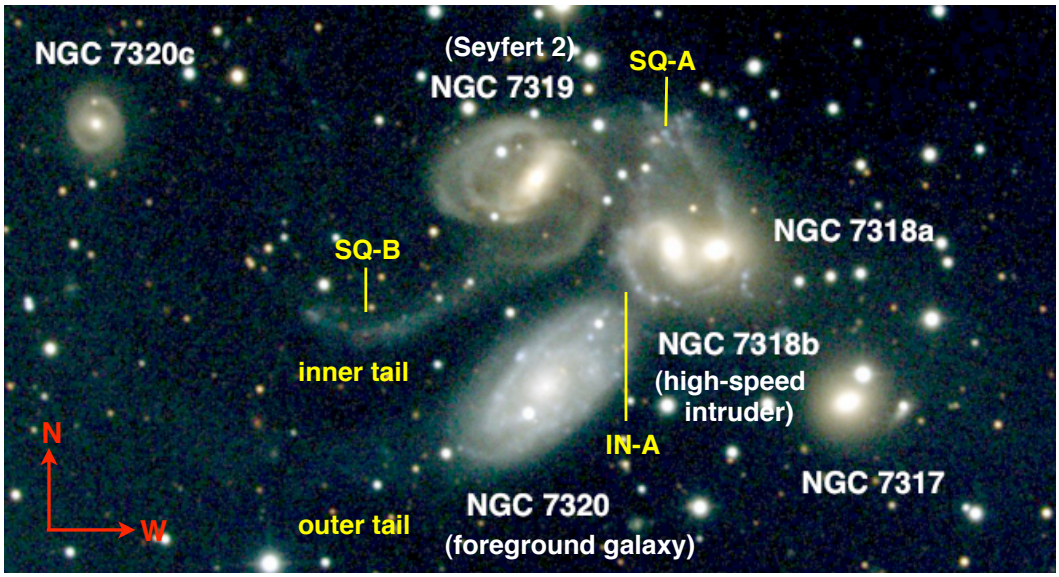

Figure 2.1 The optical morphology of Stephan's Quintet. The members and major large-scale features are marked (see text). NGC 7320 (to the lower middle in the image) is only a foreground projection. North is up and east to the left. Credit: NOAO/AURA/NSF.

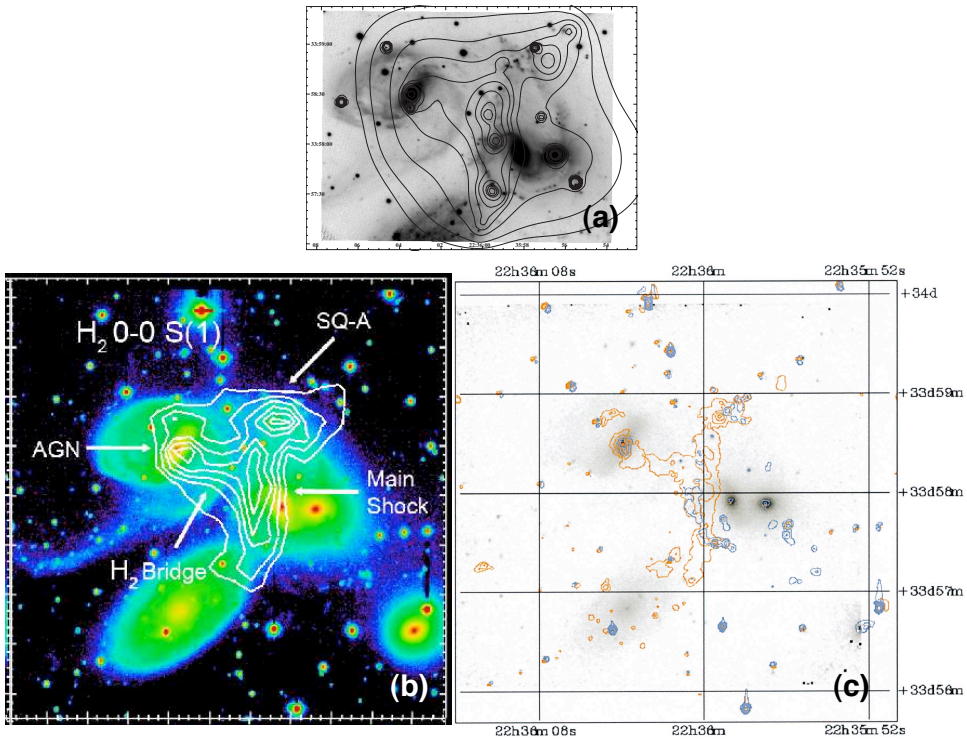

Figure 2.2 Central region of Stephan's Quintet seen in multi-wavebands: (a) a zoomed X-ray contour map (0.5∼3 keV) overlayed on a B-band image (Trinchieri et al. 2003), (b) H_2 contours on an R-band image (Cluver et al. 2010), and (c) Hα+[N II] contours (6600 km s^{-1} component shown in red and 5700 km s^{-1} component in blue) on a K′ (2.1μm) image (Xu et al. 1999). All images are in a similar scale. The huge elongated shock feature is clearly seen in the central region of the group. North is up and east to the left.

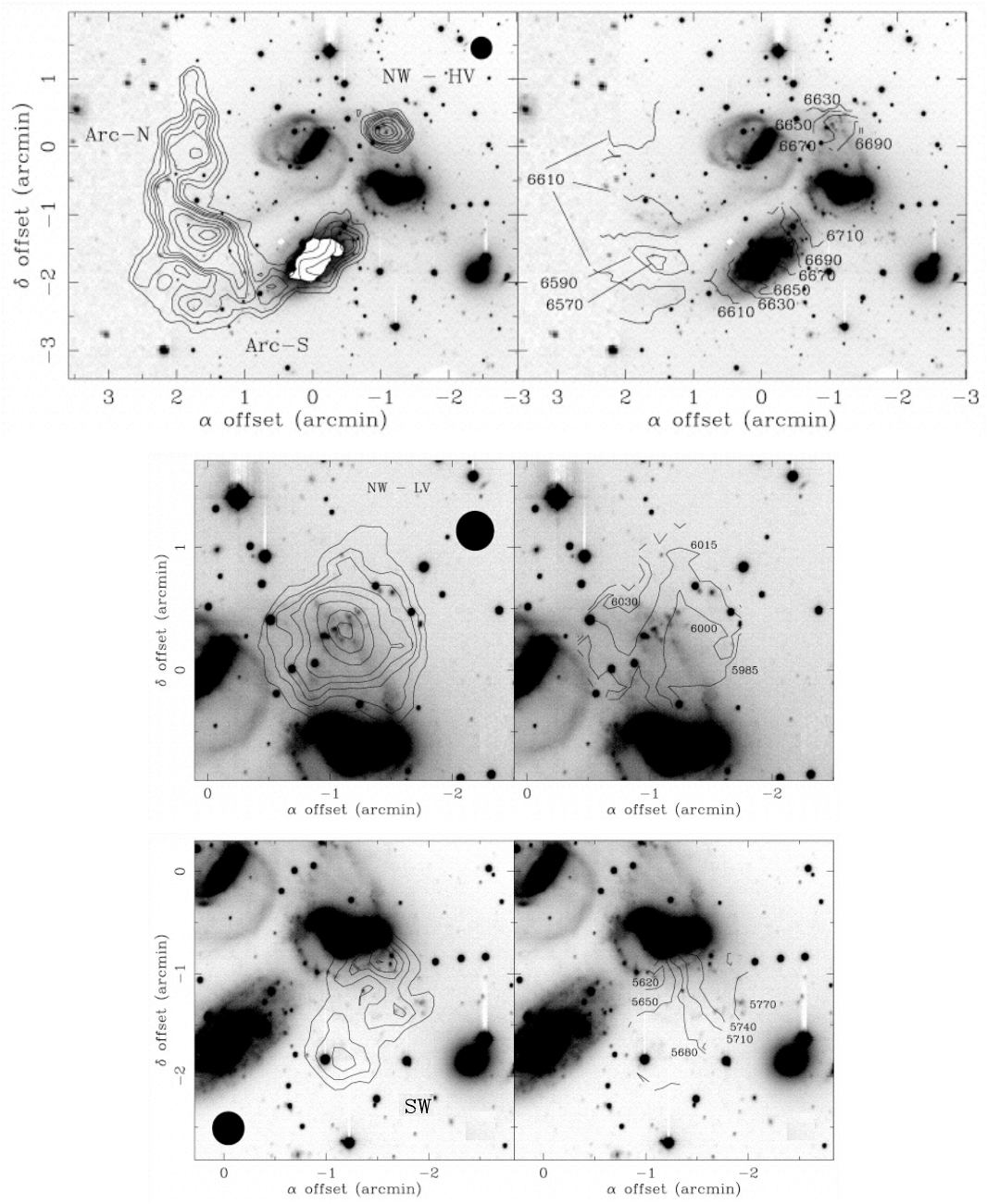

Figure 2.3 H I gas observed in Stephan's Quintet (Williams et al. 2002). The top row shows three H I clouds ("Arc-N", "Arc-S", and "NW-HV") detected in the velocity band 6500∼6800 km s^{-1} (high (radial) velocity range). The middle and bottom rows show an H I cloud ("NW-LV") observed in 5900∼6100 km s^{-1} (intermediate velocity range), and a diffuse H I feature ("SW") found in 5600∼5800 km s^{-1} (low velocity range), respectively.

SQ is a relatively close (∼94 Mpc away with a Hubble constant (H_0) of 70 km s^{-1} Mpc^{-1}) and isolated system among the Hickson's compact groups. Four members, NGC 7317, 7318a, 7319, and 7320c, have a similar recession velocity of ∼6600 km s^{-1}. In contrast, NGC 7318b has a lower recession velocity than the others by ∼900 km s^{-1}; this galaxy ("high-speed intruder") is thought to be coming toward us with the large relative velocity, having collided with the material placed between NGC 7319 and 7318a and triggering the group-wide shock shown in Figure 2.2.

The large spiral galaxy NGC 7319, whose nucleus is known to be a Seyfert 2, has a strong central bar, disturbed arms, and two long tails (hereafter the parallel tails, or the inner and outer tails; see Figure 2.1). Both inner and outer tails appear in the optical to extend from NGC 7319 toward NGC 7320c, a small spiral or ringed galaxy. The outer tail is seen at the south of the inner tail in the figure, although the outer one is harder to see as it is more diffuse and passes behind the foreground galaxy NGC 7320, running nearly parallel with the inner one. The inner tail, which is optically brighter than the outer one, is active in star formation. Many tidal dwarf galaxy (TDG) candidates have been found along the inner tail (e.g., Hunsberger 1996), including "SQ-B" marked in the figure. In ultraviolet (UV), the inner tail is far more extended toward north than in optical and shows a loop-like structure (see Figure 1 in Xu et al. 2005).

To the west of NGC 7319 (west is to the right in astronomical images), a pair of galaxies NGC 7318a/b is seen with complex features around them, including features in the NW, "SQ-A", and "IN-A" (see Figure 2.1). NGC 7318b has weakly barred spiral morphology and its optical core looks relatively intact, while its interstellar medium (ISM) has been removed, as is shown in Figure 2.3. NGC 7318a is the most difficult member for type determination. Even whether it is an elliptical or a spiral is unclear, due to the complex features around the pair. Most of the features are thought to be related to NGC 7318b, however, some of the arm-like structures might be associated with NGC 7318a (see Shostak et al. 1984). On the other hand, the photometric data of NGC 7318a show a smooth light distribution like an elliptical (Moles et al. 1998). The galaxy has generally been considered as an E.2.P. (in the Third Reference

Catalogue of Bright Galaxies (RC3); de Vaucouleurs et al. 1991), but was categorized as Sc by (Hickson et al. 1989) and SB0 by Hickson (1994). The NW features appear to cross each other, and near the apparent crossing a starburst region SQ-A has been found (Xu et al. 1999). The feature IN-A looks like a tidal tail, and some Hα clumps between NGC 7318a and 7317 might be related to IN-A.

The fifth galaxy NGC 7317 is located to the southwest of the pair NGC 7318a/b. This elliptical member does not show direct signs of interaction with others (thus the galaxy has not been included in the models). However, the diffuse optical and X-ray halos lying over the regions of NGC 7318a/b and NGC 7317 (e.g., see Figure 5 in Moles et al. 1998) indicate that the galaxy is a member of the group.

The neutral hydrogen distribution of the system is very interesting (see Figure 2.3). An H I observation using the Very Large Array (VLA) (Williams et al. 2002) found most of the gas outside of optical boundaries of the members, within five distinct components ("Arc-N", "Arc-S", "NW-HV", "NW-LV", and "SW"; shown in Figure 2.3) and in three discrete velocity bands (6500$\sim$6800 km s^{-1}, 5900$\sim$6100 km s^{-1}, and 5600$\sim$5800 km s^{-1}). The gas with higher radial velocity (6500$-$6800 km s^{-1}) is detected in two large arc-like clouds (Arc-N and Arc-S) tracing the optical inner and outer tails (see Figure 6 of Williams et al. 2002 for the view of each cloud separately) and in a relatively compact cloud (NW-HV) centered near SQ-A. Another kinematically distinct cloud (NW-LV) centered near SQ-A is observed in the intermediate velocity band (5900$-$6100 km s^{-1}); this cloud coincides with the high velocity one but is more extended. The low velocity (5600$-$5800 km s^{-1}) gas is found between NGC 7318a/b and NGC 7317 in a diffuse feature (SW).

X-ray contours (Trinchieri et al. 2003) at the central area of the group is presented in Figure 2.2(a). For the members, core regions of NGC 7319 (Seyfert 2) and 7318a generate strong to relatively strong X-ray emission. Other than the galaxies, the shock structure is clearly seen as a narrow elongated feature ("main shock") in the IGM between NGC 7319 and 7318b, embedded in more extended emission. As noted earlier, it is widely accepted that the hot X-ray-emitting gas in the elongated feature has resulted from the shock-heating triggered by

the ongoing high-speed collision between NGC 7318b (the high-speed intruder) and the IGM. The fact that the main shock occurs in a region where the cold neutral hydrogen is missing (see the top panel of Figure 2.3) also supports this idea.

The contours of rotational H_2 line emission detected in the central region are shown in Figure 2.2(b) (see also Figures 2 and 3 of Cluver et al. 2010). The strong line emission follows the X-ray emitting shock, from the starburst region SQ-A, and from the region associated with the active galaxy NGC 7319. There is another H_2 structure, which runs eastward from the main shock ("H_2 bridge"); it is also discernable in X-ray and Hα (see Figure 2.2(c)) emissions. Overall, the warm molecular gas shows a similar distribution to that of hot X-ray emitting gas. The line luminosity of the H_2 in the main shock was measured to be about three times stronger than the X-ray luminosity from the hot shocked gas, implying that H_2 lines are a stronger coolant than X-ray emission (Cluver et al. 2010).

Figure 2.2(c) shows Hα+[N II] emission in the central region of the group (Xu et al. 1999) with two different components of the emission, $\sim$6600 km s^{-1} and $\sim$5700 km s^{-1} (which is in the velocity range of the high-speed intruder) marked by red and blue colors, respectively. The 6600 km s^{-1} component shows a very similar distribution to the X-rays (Figure 2.2(a)), indicating the shock front is associated with the 6600 km s^{-1} component.

This concludes the overview of the large-scale structure of SQ. Next the origins of some major features and constraints of the models are discussed.

2.2.2 Interaction history and model constraints

The parallel tails are one of the most characteristic features resulting from past interactions in the group. Based on the shape and probable age of each tail, three different formation scenarios of the tails have been considered: (A) both tails could be generated simultaneously by an encounter of NGC 7320c with NGC 7319 (Moles et al. 1997), (B) the outer and inner tails might be produced one after one by at least two passages of NGC 7320c around NGC 7319 (Moles et al. 1997; Sulentic et al. 2001), and (C) the outer tail might be produced by an encounter of NGC 7320c with NGC 7319 and then the inner tail by a different encounter of

NGC 7318a with NGC 7319 (Xu et al. 2005).

Scenario A implies the same formation ages for both tails; a bridge and a counter tail of NGC 7319 which were supposed to be pulled out after a closest approach of NGC 7320c could later develop into the inner and outer tails, respectively. The outer tail, however, has been often interpreted to be "older" (formed earlier) than the inner tail as it is optically fainter and broader than the inner one, so this scenario has not been favored over the other two, where the outer tail is formed earlier. However, the properties of a tail (such as brightness, color, and diffuseness) would be affected by various reasons, not nearly-entirely by the time elapsed since the formation (so this scenario would be still plausible; it is applied to the models).

Scenario B considers common origins, but at different times, for both tails. It suggests a counter-tail of NGC 7319 produced by an earlier passage of NGC 7320c would become the outer tail and another tail by the recent passage become the inner tail, since each of the optical parallel tails points to NGC 7320c as a counter-tail of a victim galaxy generally curves toward the perturbing galaxy, but the more diffuse outer tail might be formed earlier. Until about a decade ago, the radial velocity difference between NGC 7319 and 7320c had been (incorrectly) thought to be $\sim$700 km s^{-1}. So, assuming a fast encounter, Moles et al. (1997) estimated the recent encounter might occur as early as $1.5 \times 10^8\, h^{-1}$ yr ago and an earlier encounter at least 5 $\times$ $10^8\, h^{-1}$ yr ago or earlier. However, more recent measurements of the radial velocity of NGC 7320c came out to be nearly equal to that of NGC 7319, which implies the recent encounter would be slow rather than fast (assuming the difference between the transverse velocities of the two galaxies is comparable to that between the radial velocities). It is thus argued that if NGC 7320c had encountered NGC 7319 producing the inner tail and moved to its current position then, assuming a slow passage, it would take at least $\sim 5 \times 10^8$ yr (Xu et al. 2005) which is much older than the previously estimated age of the inner tail (e.g., by Moles et al. 1997) but close to that of the outer tail.

In scenario C the outer tail is also formed earlier than the inner tail, as in the second scenario. The two scenarios agree on the origin of the outer tail, but not on that of the inner tail. As a solution to some of the problems raised in the second scenario regarding the non-

optical morphology and age of the inner tail, scenario C suggests an encounter of NGC 7318a might generate a counter-tail looking like the UV inner tail, and the estimated age of the inner tail by the encounter would then be about three times younger than that produced by NGC 7320c, due to the shorter distant between NGC 7318a/7319 than between NGC 7320c/7319 (Xu et al. 2005).

As described above, the origins of the inner and outer tails are not yet clearly understood. However, no matter how the parallel tails have been generated, NGC 7319 would have undergone one or more strong prograde encounters to have pulled two substantial tails out of the disk. The system appears to be strongly disturbed during the interaction, as most of gas in NGC 7319 (and the other involved galaxies) has been stripped off and huge amount of gas put into the parallel tails (see Figure 2.3).

At the time when the parallel tails were produced, NGC 7318b (the high-speed intruder) is thought to be far below the rest of the group and not to be involved in the generation of the tails. The galaxy seems to enter the group in the relatively recent past and is currently passing through the material that has been placed west of NGC 7319 with the large relative radial velocity ($\sim$900 km s^{-1}) triggering the group-wide shock.

There have been some arguments about whether or not NGC 7318b had interacted with the group (most likely with NGC 7318a) before the current collision. The optical core of the high-speed intruder looks still intact, which leads the idea that the galaxy might be entering the group for the first time (Moles et al. 1997; Sulentic et al. 2001). However, the gas disk of NGC 7318b has already been well stripped and some tail-like and ring-like features are seen around the pair NGC 7318a/b; these suggest NGC 7318b had interacted before (perhaps undergone a nearly head-on collision with NGC 7318a), because the removal of outer disks and the development of tidal features occur after the closest encounter (Williams et al. 2002; see also Xu et al. 2005).

It is very difficult to understand the origins of each of the features around the pair NGC 7318a/b clearly, due to the complex interaction(s) involving the high-speed intruder, perhaps multiple interactions from the (relatively recent) past through the present; the features might

be influenced by some hydrodynamical effects and/or tidal effects. Particularly, the features at the eastern side of the high-speed intruder would require more careful interpretations as the arms of the high-speed intruder and the main shock are very close.

The extra-nucleus starburst region SQ-A may be influenced by some hydrodynamical processes due to the current high-speed collision, because according to the Hα data the star formation in the region is occurring not only in the interstellar medium (ISM; 6000 km s^{-1} component) of the high-speed intruder but also in the IGM (6600 km s^{-1} component), and the 6600 km s^{-1} component would not be detected if SQ-A is triggered by tidal effects (Xu et al. 2003). It is worth noting that SQ-A lies nearly at the northern end of the shock ridge seen in radio continuum and at the southern end there is also a star-forming region (i.e., 7318b-south in Cluver et al. 2010) but in the ridge itself shows little star-formation (e.g., Xu et al. 2003; Cluver et al. 2010). Whether these star-forming regions just happened to be placed at the extreme ends or not (which is more likely), the mechanism of star-formation at both ends of the shock needs to be further investigated (Cluver et al. 2010).

2.3 Numerical models

An SPH code for numerical simulations of SQ has been constructed in this study. As mentioned earlier, before this hydrodynamic modeling my collaborators used an N-body code, based on primarily NEMO stellar dynamics toolbox (Teuben 1995), and performed about 3000 exploratory runs to test various interaction hypotheses and examined the gravitational aspects of the group (see Renaud et al. 2010 for details). In this new SPH modeling, all of the relatively successful N-body models have been re-tested and some additional ideas of interactions have been tried. I ran about 170 simulations with the SPH code. In this section, I first explain the SPH code details and then describe models including the modeling strategies and the differences among the models.

2.3.1 The SPH code

The SPH code used in this work has been produced by modifying the SPH code of Struck (1997) which was originally designed for studying collisions between two disk galaxies (see Struck 1997 for details), so that the code can be applied to systems with more than two galaxies. (The code of Struck (1997) has been also used for numerical studies presented in Chapters 3 and 4.) In the SPH code for SQ, four strongly interacting members NGC 7318a/b, NGC 7319, and NGC 7320c have been considered, excluding NGC 7317 (and the unrelated foreground galaxy NGC 7320), since models aimed at simulating the group from the generation of the parallel tails to the near future; during which time the effect of NGC 7317 on the group is small (e.g., Moles et al. 1997).

Each model galaxy consists of two disks with gas and collisionless star particles and a rigid dark matter halo. The elliptical looking member NGC 7318a is also initialized with disks, but some initial parameters (such as the angular and random velocities of its test particles) are adjusted to be modeled as an elliptical galaxy.

In the SPH code, hydrodynamical forces are calculated with a spline kernel on a grid (see Appendix A for details). A constant smoothing length and fixed unit cells in a grid are used. Local self-gravity is calculated between gas particles in adjacent cells. A standard artificial viscosity formulation and a simple leapfrog integration method are used. The large-scale dynamics of interactions are simulated with a restricted three-body approximation. The specific form of the halo acceleration of a particle is

$$a = \frac{-GM_h}{\epsilon^2} \frac{r/\epsilon}{(1 + r^2/\epsilon^2)^{n_h}}, \tag{2.1}$$

where M_h is a halo mass scale, ϵ is a core radius, and the index n_h specifies the compactness of the halo.

Simple treatments of heating and cooling are included for gas particles using an adiabatic equation of state. (For pressure calculation, adiabatic equation of state was assumed. Heating and cooling calculated separately. Constant cooling timescales used in three temperature ranges as described in Struck 1997.) Star formation is assumed to occur when the local gas

density exceeds a constant threshold density and the gas temperature goes below another constant threshold temperature. The density and temperature thresholds are arbitrary and can be normalized to give realistic star formation rate for the system. (The code's density threshold is low compared to that in real galaxies, because of the limited resolution. However, it is qualitatively correct in forming stars in the densest regions.) Dynamical friction (see Binney & Tremaine 2008) is not included for the current models. The effects of dynamical friction will be added for later models; with which the future evolution of SQ will be studied.

The code uses the non-inertial reference frame of a "primary" galaxy. (The model galaxy for NGC 7319 has been chosen to be the primary). All masses and lengths in the code are scaled to the halo mass scale (M_h in Equation 2.1) and the core radius (ϵ in Equation 2.1) in the halo potential of the primary galaxy. There is a characteristic sound speed in the code; which is used as a unit velocity. These code units are dimensionless and have been converted to the physical units after simulations (described in the following subsection).

There are fixed spatial boundaries imposed in the code. The boundaries are large enough to include almost all particles but not too big for efficient computing performance. A few distant particles reach the boundaries and are excluded from the simulations.

2.3.2 Model differences and initial conditions

Most of SPH simulations are run from just before the production of the parallel tails to shortly after the current high-speed collision. I divided the modeling efforts in three major stages, each with a specific goal: (1) to reproduce the inner and outer tails in a good configuration, stripping much of gas off the involved members, (2) to test the occurrence of any intermediate interaction before the present, especially between the high-speed intruder and NGC 7318a, and (3) to make a high-speed present-day collision between NGC 7318b and the IGM of the group. (These three stages do not have strict boundaries and can overlap; they are more like conceptual categories, though several interactions in the group do indeed seem to occur sequentially.) I will henceforth refer to the model galaxies for NGC 7319, 7318a, 7318b (the high-speed intruder), and 7320c as G1, G2, G3, and G4, respectively to avoid confusion

between the model galaxies and the real ones.

Various interactions have been attempted at each stage. In particular, I spent more time at the first stage than the other two to generate the two tidal tails (which are supposed to develop as the parallel tails) out of the disk of G1. The parallel tails are one of the most distinctive features resulting from the past interactions in the group, so a good model of SQ should be able to reproduce them, and the outcome of the first stage would directly affect the interactions at the later stages. The models attempting to reproduce the parallel tails at the first stage were evaluated depending on how reasonably they reproduced the two tails, and those models that successfully generated the tails were evolved further. Once I had any complete model that reproduced the overall morphology of the system relatively well throughout the entire stages, I then made several similar models changing the values of a few model parameters and ran them again to determine how the models are affected by particular parameter values.

I tried many models to produce the parallel tails in both scenario A (with one encounter of G4) and C (with an encounter of G4 and then an encounter of G2), but not on scenario B (with at least two encounters of G4) as the previous N-body simulations (which included the effects of dynamical friction; Renaud et al. 2010) already found that scenario B does not work properly. (I will hereafter describe complete models as "models A" or "models C" depending on which model scenario is referred to.) The reason why the N-body models with scenario B failed was: after one tail (the outer tail) had been produced by the earlier encounter, G4 had to encounter G1 again *very closely* to be able to generate another tail (the inner tail), but then G4 could not leave G1 far enough toward its current position (actually, G4 collapsed into the larger member G1 in most cases) due to the strong gravitational attraction and the dynamical friction.

In the N-body simulations, one of models C was chosen as the best model in reproducing the general stellar morphology of SQ. In the SPH simulations, however, models A came out generally better than models C. The differences between the N-body and the SPH modeling are primarily due to the different halo potentials used in each simulation code and besides, SPH models are evaluated not only on the basis of the stellar, but also the gas features. I will

explain more about models A and C, including the advantages and disadvantages of each type, in the next section when I present the model results.

I finish this subsection by stating initial parameters used in one of the most satisfying SPH models A (the fiducial model). Many details of the fiducial model are summarized in Table 2.1. The values in the table were derived from observational data or modeling experiences with many number of trials. Those values are presented in the physical units. To scale the SPH code, the length and velocity code units have been converted to 1.0 kpc and 5.0 km s^{-1} in all models, then the time code unit becomes 200 Myr. The mass code unit, which is the halo mass scale M_h for G1 (see Equation 2.1), has been scaled to $4.7 \times 10^{10} M_\odot$ in most models including the fiducial model; M_h for G2, G3, and G4 relative to that of G1 have been chosen to be 0.78, 0.62, and 0.22, respectively. ϵ and n_h in Equation 2.1 for all members have been set to 1.0 kpc and 1.4 in the fiducial model. There has been a halo cut-off radius assigned for each member in the fiducial model as 135 kpc (G1), 55 kpc (G2), 80 kpc (G3), and 45 kpc (G4); which is five times larger than either the gas disk radius (for G1, G3, and G4) or star disk radius (for G2, which has been set with a smaller gas disk than its star disk). The halo mass, with the given potential (Equation 2.1), for each member out to the cut-off radius, in the unit of $10^{10} M_\odot$, is 12.6 (G1), 8.2 (G2), 7.1 (G3), and 2.4 (G4). No group halo has been assigned. The initial gas disk of each member in the model (from G1 through G4 in order) were set to 27 kpc, 8 kpc, 16 kpc, and 9 kpc, and the initial stellar disk to 18 kpc, 11 kpc, 11 kpc, and 7 kpc. So, the stellar and gas disk sizes of the least massive member G4 was chosen to be about one third of those of the most massive member G1. G2 and G3 were selected to be comparable in mass and stellar disk size, but not in gas disk size. G2 was set to have smaller gas disk with a lot fewer gas particles compared to G3. In all models, all galaxies were initialized in the x-y plane (which was chosen to be equivalent to the plane of the sky) with the disk spins in either clockwise or counter-clockwise directions, and then rotated around any of the three orthogonal axes as necessary. In the fiducial model, G1 and G4 were set with counter-clockwise directional spins, while G2 and G3 with clockwise directional spins. All members in the fiducial model were not rotated around any direction. (The members might not be all exactly face-on, but tilts were

Table 2.1 Initial parameters of the fiducial model

	G1	G2	G3	G4
Halo masses[a] ($\times 10^{10} M_{\odot}$)[b]	12.6	8.2	7.1	2.4
Halo cutoff radii[c](kpc)	135.0	55.0	80.0	45.0
Gas disk radii (kpc)	27.0	8.0	16.0	9.0
Stellar disk radii (kpc)	18.0	11.0	11.0	7.0
Gas particle numbers	68,680	6,000	24,000	7,480
Star particle numbers	32,000	11,760	11,760	4,960
Disk orientations[d]		180° about x-axis	180° about x-axis	
Initial center positions[e] (x,y,z) (kpc)	at origin	(−70.0, 10.0, −20.0)	(12.0, 2.0, −340.0)	(12.5, −15.3, 15.3)
Initial center velocities [f] (v_x,v_y,v_z) (km s^{-1})	(0.0, 0.0, 0.0)	(110.0, −27.0, −72.5)	(20.0, −7.5, 300.0)	(35.9, 79.5, −77.5)

[a]The given halo mass is that contained within a halo cut-off radius. Gas and star disk masses are negligible in this model; see text.

[b]Physical units used in this table. Conversion from code units described in text.

[c]In this model, the halo cut-off radii for G1, G3, and G4 are set to five times their gas disk radii; for G2, five times its star disk radius. No group halo is applied.

[d]All galaxy disks are initialized in the x-y plane and then rotated as necessary. In this model, G1 and G4 are set in the x-y plane with counter-clockwise directional spins, and G2 and G3 with clockwise directional spins. No additional tilts are applied in this model.

[e]Coordinates defined in a conventional, right-handed frame, with the origin fixed at the center of the primary, G1. The x-y plane is defined as the plane of the sky, and positive z as the direction towards the observer.

[f]Positive z velocities are towards us.

ignored in the fiducial model; different tilts particularly for G3, the high-speed intruder, were tested in several similar model to the fiducial model for comparison).

2.4 Simulation Results

In this section I present the results of SPH models. I first describe the general evolution of the fiducial model, as a representative for models A, focusing on the generations of the large-scale structural features in the system. Then I compare models A to models C, discussing the advantages and disadvantages of the models. Finally, I analyze the gas properties in the fiducial model and compare to observations.

2.4.1 Evolution of the fiducial model

The fiducial model is designed firstly to generate the inner and outer tails simultaneously by a close encounter of G4 with G1 (as suggested in scenario A in Section 2.2.2), then at the second stage to have a collision between G2 and G3 relatively far below the plane of G1,

and finally at the third stage to make a high-speed collision between G3 and the material found west of G1 (c.f, for the description of the modeling stages see Section 2.3.2). The initial parameters and the subsequent orbits of the model galaxies are presented in Table 2.1 (see also Section 2.3.2) and Figure 2.4, respectively. The distributions of star and gas particles of the model galaxies at four times are shown in Figures 2.5 through 2.8: star particles projected on to the x-y plane in Figure 2.5, and on to the x-z plane in Figure 2.6; gas particles projected on to the x-y plane in Figure 2.7, and on to the x-z plane in Figure 2.8.

As mentioned earlier, the coordinate system that moves with the halo center of G1 (the most massive and largest member in the model) is used in the SPH code, so the galaxy appears fixed at the origin throughout the simulations, and the x-y plane is defined as the plane of the sky in all models. The disks in the fiducial model are initialized with star and gas particles as described in Table 2.1. The code's length and velocity units are scaled to 1.0 kpc and 5.0 km s^{-1} in all models. The time code unit is then 200 Myr. Note, however, that this (representative) scaling is not exact; the factors could be increased or decreased.

The fiducial simulation starts shortly before G4 makes its closest approach to G1. As shown in Figure 2.4, G4 starts southwest vicinity of G1 seen in the sky plane, swings closely around G1 in a counter-clockwise direction, and moves toward east. Seen from the sides, G4 starts a little bit above G1, turns quickly around G1 going downward, and then slows in the vertical direction as it moves toward east. On the other hand, G2 starts far from G1 and moves toward west going deeper below G1. (This orbit of G2 has been chosen in such a way that G2 has little to no effect to the development of the parallel tails, which were supposed to be generated by an encounter of G4 with G1, staying relatively far from both tails until they grow well, and then G2 can encounter with G3 well below the plane of G1). G3, the high-speed intruder, has been started far below all the others, set to move nearly vertically toward the rest of the group, meet with G2 on its way up, and then pass through between G1 and G2 at a high speed.

The top-left panels in Figures 2.5, 2.6, 2.7, and 2.8 show the early development of the inner and outer tails at about $t = 1.9$ units or 380 Myr (in the representative scaling) after the closest encounter of G4 with G1. (Time is measured from the instant of the closest approach between

G1 and G4 throughout this chapter for convenience; the start of the model is at about -1.0 in code time units.) By this time G4 has swung around G1 in a counter-clockwise direction passing through the large disk of G1 from front to behind and has pulled two massive arms (a bridge and a counter-arm) out of the disk of G1. Since the initial disk spins of both G1 and G4 have been set in counter-clockwise directions (as presented in Table 2.1), both galaxies feel the encounter as prograde. The early encounter between G1 and G4 in this model is somewhat similar to that between M51 and NGC 5195 proposed by Toomre & Toomre (1972) in their numerical model. (Not only the orbit but also the mass of the companion relative to the main galaxy is similar in both models, as 0.22 in our model and 0.25 in their model). However unlike their model, the small companion G4 in our model directly contacts the larger member G1, bringing stronger tidal damage on both galaxies. As seen in the first snap shots in the four figures, both galaxies have been strongly disturbed by the collisional encounter; many test particles of the galaxies have been stripped off or transferred to the other galaxy. In general, gas tends to be affected more by the encounter than the stars. As a related difference, a lot more gas particles from G4 than star particles are seen to be captured by G1 (compare the top-left panels in Figures 2.5 and 2.6 to those in Figures 2.7 and 2.8). The accreted gas at the central region of G1 during the encounter might play a role to the development in G1 as an active galaxy (as NGC 7319 has been found to have a type 2 Seyfert nucleus).

The two arms drawn out of G1 continue to grow through the time shown in the top-right panels in the four figures ($t = 660$ Myr), forming a parallel configuration. As intended in this model, G2 does not distort the tails while they develop since it stays far from them; meanwhile, G3 continues to approach the group. At the instant of the snapshots, G3 is about to collide with G2 at $z \sim -70$ kpc in the adopted scaling. Here G2 is placed slightly to the west (the positive x direction) of G3 at the onset of the collision. This is intended to make a partial head-on collision between G2 and G3, and to stabilize the orbit of G3 between G1 and G2, keeping G3 from being attracted too much toward G1 afterward, even though the effect would be small due to the high vertical velocity of G3. Note that I am not completely certain whether this collision between G2 and G3 does in fact occur (and in the way tried in the model). The

collision at the second stage in the model has been attempted based on the interpretation that some of the disturbed features observed around the pair NGC 7318a/b (see Section 2.2.2) could be the result of the earlier interaction between the two galaxies. It is thought that some features, such as IN-A and stripped gas of G3, might have tidal origin that require some time (about 100 Myr) to develop to the presently observed state.

The lower-left and lower-right panels in the four figures (Figures 2.5 through 2.8) show the model system at the times near present, during the high-speed collision between G3 and the IGM (t = 890 Myr $\equiv t_3$; shortly before the present) and shortly after the collision (t = 1070 Myr $\equiv t_4$; shortly after the present), respectively. The materials which G3 collides with are mostly part of the outer tail. Since G3 collided with G2 earlier it has been evolving tidal structures. G3 in this model develops moderate tidal tails by the onset of the current collision, so the disk and the tails pulled out of it both hit the IGM at a high-speed (the vertical speeds of the model galaxies will be discussed in Section 2.4.3).

The morphology of the model at $t_3 \sim t_4$ looks generally similar to that of SQ. First of all, the positions of the four model galaxies projected onto the x-y plane are close to those observed. The parallel tails look similar to the observed features as well. It should be emphasized that even though the inner and outer tails in the model were generated simultaneously, the inner tail appears stronger than the outer tail in stellar features. Some of the stellar features around NGC 7318a/b were generated very roughly in the model: The two tails drawn out of G3 (by the collision with G2) do not match with the real optical features very well. However, the one extracted from the eastern side of the disk looks similar to the feature IN-A, although the curvature and orientation are not quite right. A feature like SQ-A is produced at the north of G3; the feature began to be formed shortly after G3 started to impact the IGM and has grown quickly with time (it is quite small at t_3, but larger at t_4; see also Figure 2.9). The gas structure will be compared later in Section 2.4.3.

2.4.2 Models A versus models C

The fiducial model described above is one of models of type A (which are designed to generate the inner and outer tails simultaneously by an encounter of G4 with G1 as suggested in scenario A in Section 2.2.2). The observations of the inner and outer tails in SQ suggest a younger age of the inner tail than the outer tail (e.g. the inner tail is optically brighter, bluer, and thinner). I thought at the beginning of this work that models C (which intend to generate the outer tail first by an earlier encounter of G4 with G1 and then the inner tail by the recent encounter of G2 with G1 as suggested scenario C) would be more appropriate for the system. However, as I proceeded with the simulations, I found difficulties with models of type C.

First of all, reconstructing two long tails one after one in a good configuration following scenario C was much more complicated than I expected. In such models, producing the outer tail first from G1 by a close encounter of G4 and letting G4 leave toward east (to its current position) are easy, however, because the scenario assumes the inner tail is formed sufficiently later than the outer tail, G2 has to encounter G1 closely (to produce the inner tail) *after the previously generated outer tail has already been grown.* Then, even though G2 could manage to pull the inner tail out of (the already disturbed) G1, creating a relatively good configuration with the outer tail, G2 at the same time strongly distorts the outer tail. This "dilemma" (G2 has to pass G1 closely to produce the inner tail but then it also destroys the outer tail) occurred in the earlier N-body models as well, so they devised a very inclined orbit of G2 with which G2 would not disturb the outer tail (see Renaud et al. 2010 for details). I applied the similar orbits for G2 in models C, but the effect of G2 on the outer tail was still too strong due to the extended halo potentials used in the SPH code (see Equation 2.1). To decrease the effect of G2 on the outer tail, I tried particularly smaller cutoffs for the halo potentials of the model galaxies. (I cut off each halo potential at 2∼3 times the maximum initial disk extent for models C, and 5 or more times of that for models A; no group halo applied in all models).

Another disadvantage of models C is that it is hard to adjust the orbit of G2 after it encounters G1 to best fit later developments. I prefer to place G2 relatively far below at the second stage so it collides with G3 (like in the fiducial model), and so G3 has time to develop

tidal features (assuming some features of NGC 7318b have tidal origins). However, when G2 is placed on an inclined orbit to make the inner tail without destroying the outer tail at the first stage, it is difficult to put G2 sufficiently far down at the second stage and then let G2 slow down in its vertical motion at the third stage (as it should have a small vertical velocity relative to G1 near the present). Moreover, apart from the possibility of the collision between G2 and G3 well below the plane of G1, it is difficult to evolve sufficiently many particles to the western side of G1 to be hit and shocked by G3 at the third stage in these models.

Models of type C do have some advantages. One is that the observed gas distribution near the parallel tails could generally be well reproduced. Another is that a transient feature like the observed H_2-bridge could be easily generated by the encounter of G2 with G1 in models C. I, however, have not tried to optimize models C as thoroughly as with models A. Thus, I cannot entirely rule out models C (scenario C).

2.4.3 Gas properties

I first compare the kinematical and structural features of gas formed in the fiducial model at t_4 (the time of the lower-right panels in Figures 2.5 through 2.8) to the observed H I features in three different velocity ranges (see Figure 2.3). At that time, the vertical velocities of the centers of the model galaxies G2, G3, and G4 (relative to G1) are -3.6, 64.7, and -3.3 in code units, respectively. (G3 has much more higher vertical velocity than the others, however, its vertical speed is not fast enough to be comparable to the observed value ($\sim$900 km s^{-1}) with the representative scaling. I found that other models with different vertical velocities for G3, ranging from slightly lower to twice higher than that in the fiducial model, have similar results as long as G3 has a much higher vertical velocity than the others). I will hereafter use "v_z" for the vertical velocity of a test particle in the non-inertial reference frame of G1 (used in all SPH models), and "v_r" for an observed radial (line-of-sight or recession) velocity. To compare with the H I features in each v_r range, I roughly divide the gas particles from the model with v_z into three ranges (see Figure 2.9): $v_z < 20$ (high-v_r), $20 \leq v_z < 55$ (intermediate-v_r), and $v_z \leq 55$ (low-v_r). In contrast to the H I observation (where almost no gas was detected in the central

regions of all members), SPH models (both types of models A and C) did not remove most of the gas from the members. However, some other structural features of gas were reproduced relatively successfully in the fiducial model.

As shown in the top row of Figure 2.9, the gas corresponding to the high-v_r range consists of particles originating from mostly G1, G2, and G4 (which have a similar high radial velocity themselves) as expected (note that G2 was initially set with the smallest number of gas particles as indicated in Table 2.1). A few particles originating from the high-speed intruder G3 (3.5% of G3 gas particles) are captured by the others or scattered into the intergalactic space are in this v_r range. Many high-v_r gas particles are found between G1 and G4, tracing the stellar parallel tails (see the lower-right panel of Figure 2.5). These groups of gas particles in the model look quite similar to the two huge arc-like H I clouds observed along the optical inner and outer tails in high-v_r range (Arc-N and Arc-S in Figure 2.3, respectively). Arc-S extends well beyond the southern tip of the optical outer tail, and the gas feature formed in the model along the outer tail extends further than the corresponding stellar feature. Arc-N curves toward north (as the UV inner tail; see Section 2.2) rather than toward NGC 7320c. In the model many gas particles distributed along the inner tail seem to be curved toward G4. However with a careful look, there is a trail of gas curved far to the north like the observed cloud Arc-N. Another notable high-v_r gas feature is seen in the top row of the figure (see the left panel) at east of G1 and north of G3. I interpret this gas as the compact high-v_r H I cloud (NW-HV) detected near SQ-A, although the model feature should be separated more from both G1 and G3. (I tried to refine the feature in some similar models by using different values of v_z and/or tilt for G3. However with the limited resolution, the feature did not come out noticeably differently.)

Gas particles in the intermediate-v_r range (see the middle row of Figure 2.9) appear mostly at north of G3. Most of these gas have come from either G1(35%) or G3 (63%) (note that the percentages vary quite a lot depending on the criteria for dividing the v_r ranges; it is also affected by the number of gas particles set in each member). The observed intermediate-v_r H I cloud (NW-LV) coincides with the high-v_r cloud (NW-HV) near SQ-A, but more extended. The intermediate-v_r gas particles in the model are distributed over a larger area than the high-

v_r gas particles at north of G3.

The gas particles in the low-v_r range are presented in the bottom row of the figure. Almost all (99%) of the particles originate from G3 (87% of G3 gas particles are in this range). The H I observation found low-v_r gas in south of NGC 7318a/b diffusely distributed (the feature SW in Figure 2.3), and no gas at the central area of G3. As pointed out earlier, in contrast to observation, many gas particles in the model remain in the disk of G3 and the spiral features look somewhat different. However, some of the particles found south of G3 appear more or less similar to the diffuse H I gas.

Next I briefly describe hot gas distribution from the fiducial model at t_3 when G3 hits the IGM. The particles shown in the left panel in Figure 2.10 are those hot to warm gas exceeding a certain (arbitrarily chosen) common temperature cutoff, in the high-v_r range at the time; about 17% of the total gas particles have higher temperatures than the cutoff at the time, but it decreases to about 6.6% at about 0.35 time unit (70 Myr) before and after t_3 with the same cutoff. In the right panel of the figure, I display the star forming gas particles of the model at t_3 to compare the distribution of the hot to warm gas to that of the star forming gas. Even though the model results in the figure are too rough to be able to specifically compare to observations, due to the simplified treatment of heating and cooling in the code, we can see an elongated feature of hot gas particles, with little star formation in the area of the elongated feature. This implies that the elongated feature in the model would be heated by the collision with G3 rather than by star formations, in agreement with the observations, and a significant result of the hydrodynamic modeling.

2.5 Summary and discussion

Motivated by the disturbed structure of SQ, including the remarkable group-wide shock seen at the IGM between NGC 7319 and 7318a, and using published high quality observations for the system in various wavebands, I have attempted to model the interaction history and the evolution of the large-scale structure of the group.

Despite of complex interactions expected in the compact group, some of its major features

allow one to constrain the models reasonably well. First, the appearance of the parallel tails provides important clues to track how they were formed, narrowing down the possibilities to encounters of NGC 7320c and/or NGC 7318a with NGC 7319. In addition, the fact that such delicate tidal features extend large distances outward justifies the supposition that members might not pass close to the tails after they were produced, otherwise they would have been destroyed or greatly modified. Some of the other complex disturbed features around the pair NGC 7318a/b, such as the tail-like feature IN-A and the stripped gas disk of the high-speed intruder, suggest NGC 7318b might have interacted with NGC7318a before. At the current time, it is known from many observations that the high-speed intruder, NGC 7318b, has hit IGM giving rise to the large-scale shock.

The interactions described above seem to take place one after one, involving mainly two members at a time; which simplifies the modeling. Thus I divided each of the models in three major stages and simulated a series of plausible interactions in order: At the first stage, I tried a collision between NGC 7319 and 7320c to produce both of the parallel tails simultaneously in models (models A), or via an encounter between NGC 7319 and 7320c to generate the outer tail first and then an encounter between NGC 7319 and 7318a to pull out the inner tail later (models C). Then I attempted at the second stage an interaction between NGC 7318a and 7318b of varying intensity, and at the final stage a collision between NGC 7318b with IGM.

Models A were generally more successful than model C. Even though generating the parallel tails one by one from two different interactions seems to be conceptually reasonable, in models C it turned out to be very difficult to pull another substantial tail (the inner tail) in a second close encounter, while at the same time preserving the outer tail. This later encounter usually destroyed the outer tail in models with extended halo potentials, and with very limited halos it still disturbed the outer tail, yielding a poor tail morphology. On the other hand, a single strong encounter, as in models A, could generate two substantial tails nicely.

The fiducial model (presented in the previous section) is generally successful at reproducing the large-scale morphology and kinematics. Specifically, the current relative positions (projected onto the sky plane) and radial velocities of the four members, the long parallel tails with

thinner and brighter inner tail in stellar feature, the huge amount of high-v_r gas along both of the parallel tails, the stellar features looking like IN-A and SQ-A, the high and intermediate-v_r gas at north of the high-speed intruder and some scattered low-v_r gas at southwest of the high-speed intruder that were produced in the model resemble more or less the real features. However, the gas removal from each disk, the many disturbed structural features around NGC 7318a/b, and the detailed inner structures of the spiral members were not reproduced in SPH models. The gas temperature and star-formation history of the models are not accurate enough for detailed comparison to observations. The shortcomings of the models are the result of limited resolution and the approximate treatments of heating and cooling in the current code. Dynamical friction has also been neglected in this work, though the effect would not change the main results, it becomes particularly significant to model the future of the system.

Finally, I note some ramifications from this work. Numerical modeling of compact groups would have more difficulties and uncertainties than binary systems in deducing the dynamical history and adjusting all the model parameters, however, for some groups like SQ with very extended features (preserving delicate, extended tidal structures as well), the models of those groups could be well constrained and modeling could be much simplified to attempting a sequence of two-at-a-time collisions. There are some other systems among the Hickson's compact groups which show extended features; SQ may be the prototype of the groups. The dynamical evolution of these groups can be studied more in depth with numerical simulations in similar ways attempted in this work. This would also help to better understand the formation/evolution of the high redshift galaxies.

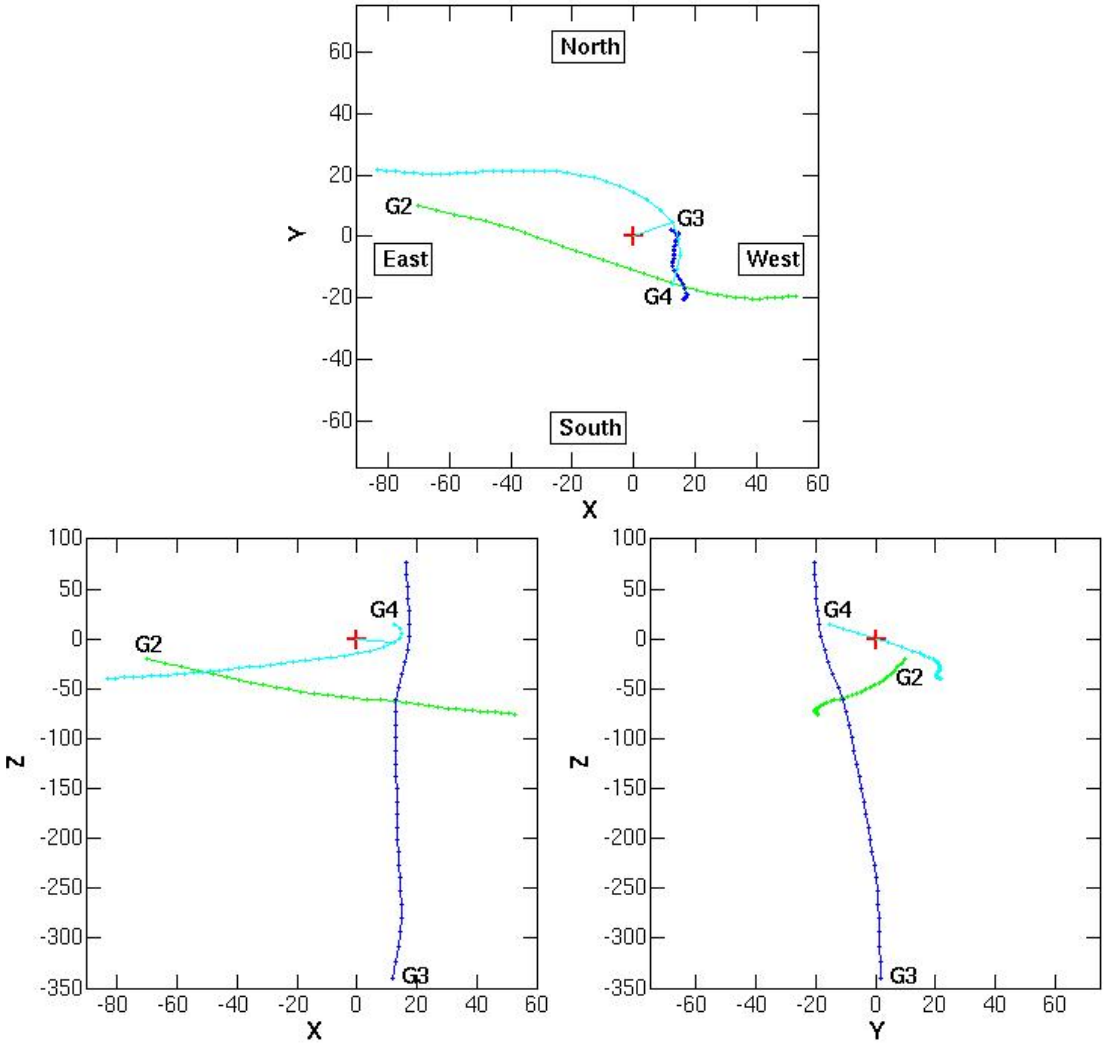

Figure 2.4 The trajectories of the four model galaxies in the fiducial model. The top, bottom-left, and bottom-right panels show the trajectories projected on to the x-y plane (i.e. plane of the sky), the x-z plane, and the y-z plane, respectively. Red, green, blue, and cyan are used to represent the center positions of the halo potentials of G1, G2, G3, and G4, respectively. G1 is fixed at the origin (marked with a red cross) throughout the simulation. Near the initial positions of the other three members (see Table 2.1), the galaxy names (G2, G3, and G4) are indicated. Little knots marked in the orbital trajectories show the positions of the model galaxies at every output step, which is not fixed, ~ 0.25 time unit (1 code time unit is 200 Myr in the representative scaling). The closest approach between G1 and G4 is indicated with a cyan line. The axes are marked in code length units (1 code length unit is scaled to 1 kpc).

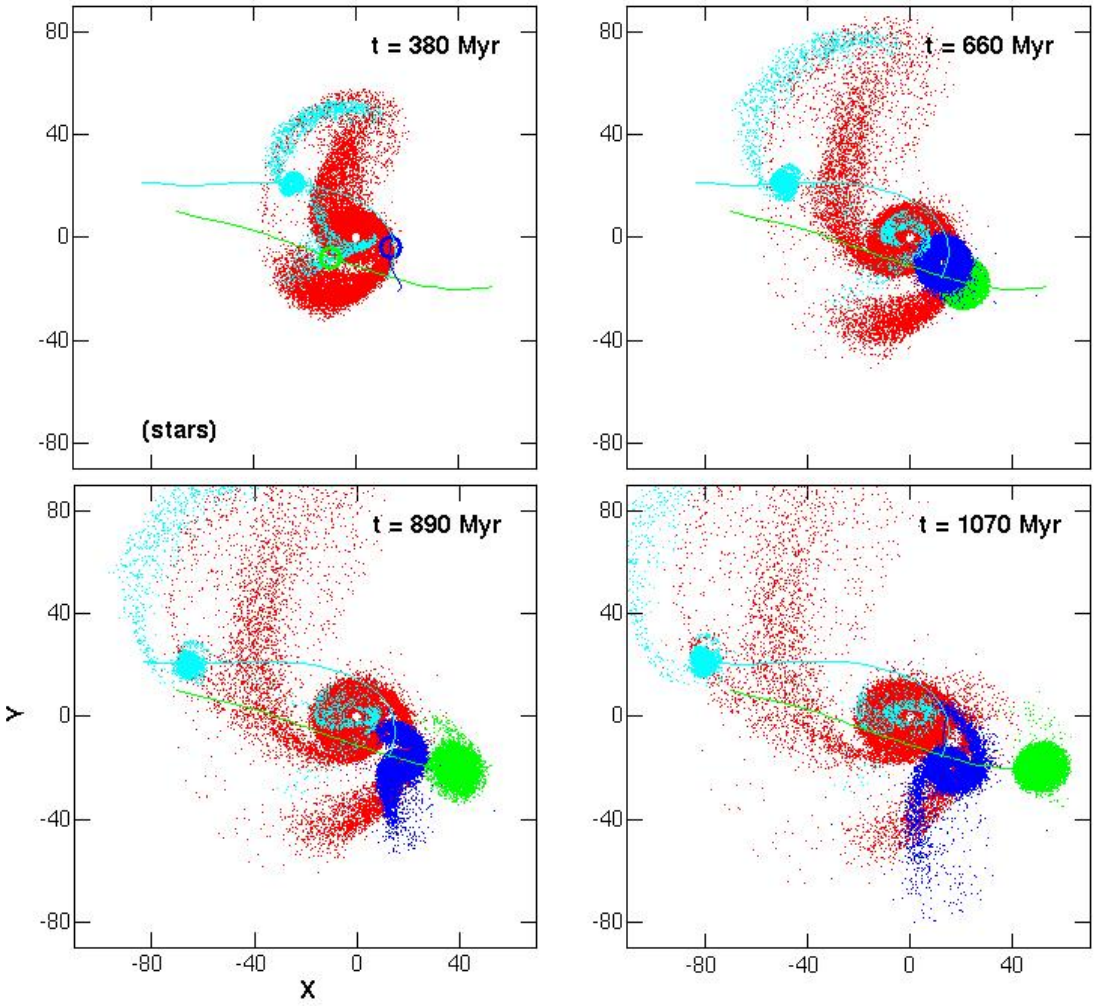

Figure 2.5 Four snapshots from the fiducial model of star particles projected on to the x-y plane. In each panel, particles originating from G1, G2, G3, and G4 are plotted with red, green, blue, and cyan dots, respectively (the red dots were plotted at first and then green, blue, and cyan dots in order). The orbital trajectories (see Figure 2.4) of the members are overlaid in the same colors used for the particles. Time indicated in each panel is measured from the closest approach between G1 and G4. In the top-left panel, the star particles of G2 and G3 are not displayed in order to show the bridge and counter-tail pulled out of G1 clearly (instead, the center positions of G2 and G3 are indicated with small green and blue rings). The top-right panel is at the onset of the collision between G2 and G3 (see Figure 2.6 for the view in the x-z plane). The bottom-left and bottom-right panels are at times near the present (shortly before and after the present) when G3 is colliding with the particles placing between G1 and G2, and when G3 has collided through the particles, respectively.

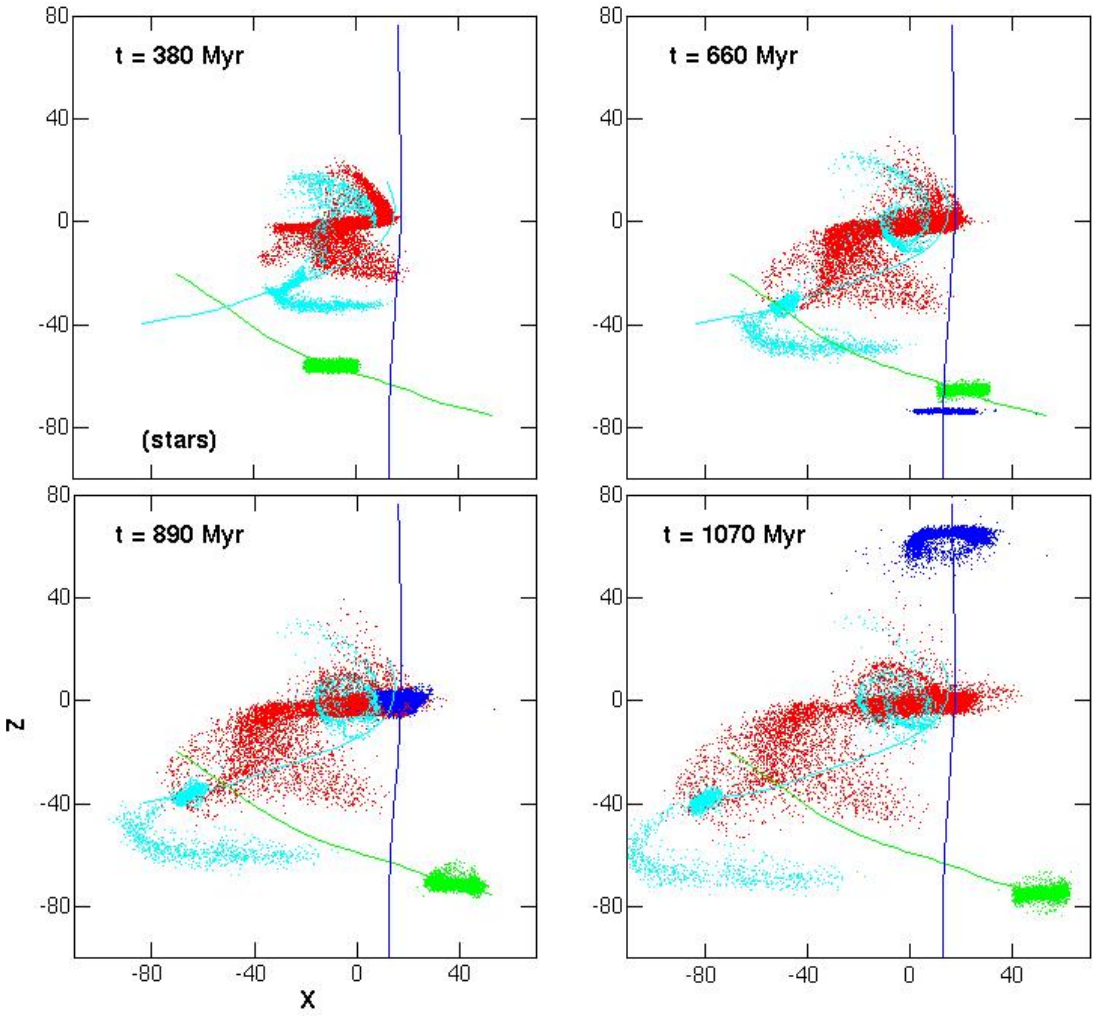

Figure 2.6 Four snapshots from the fiducial model of star particles projected on to the x-z plane. These are the same snapshots to those in Figure 2.5, showing from the side. Colors are used in the same ways in Figure 2.5 (red for G1, green for G2, blue for G3, and cyan for G4). In the top-left panel, G3 is not shown as it is at z $\sim -$ 160.

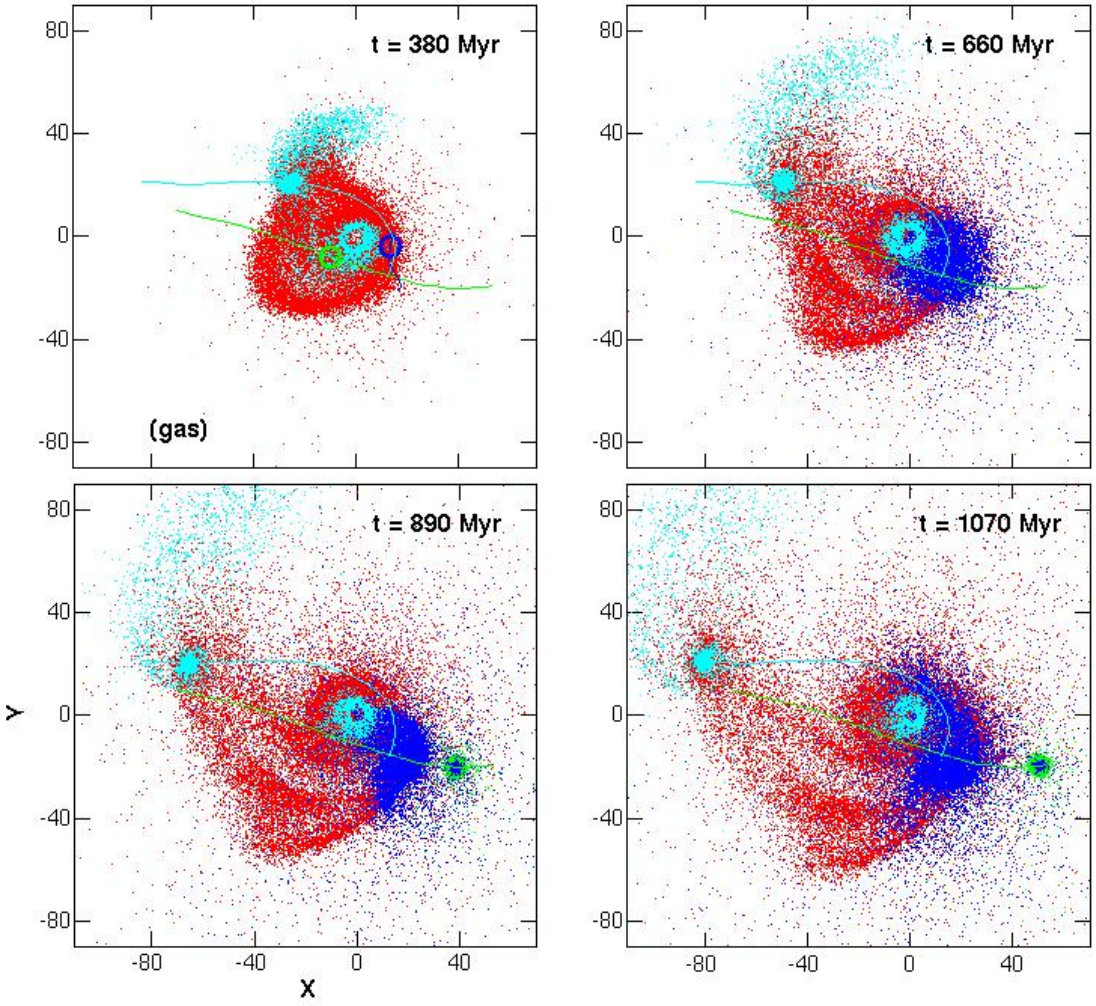

Figure 2.7 Four snapshots from the fiducial model of gas particles projected on to the x-y plane. These snapshots are taken at the same times to those in Figure 2.5, showing the distribution of gas particles. Colors are used in the same ways in Figure 2.5 (red for G1, green for G2, blue for G3, and cyan for G4). In the top-left panel, the gas particles of G2 and G3 are not displayed in order to show the bridge and counter-tail pulled out of G1 clearly (instead, the center positions of G2 and G3 are indicated with small green and blue rings). The views in the x-z plane are presented in Figure 2.8.

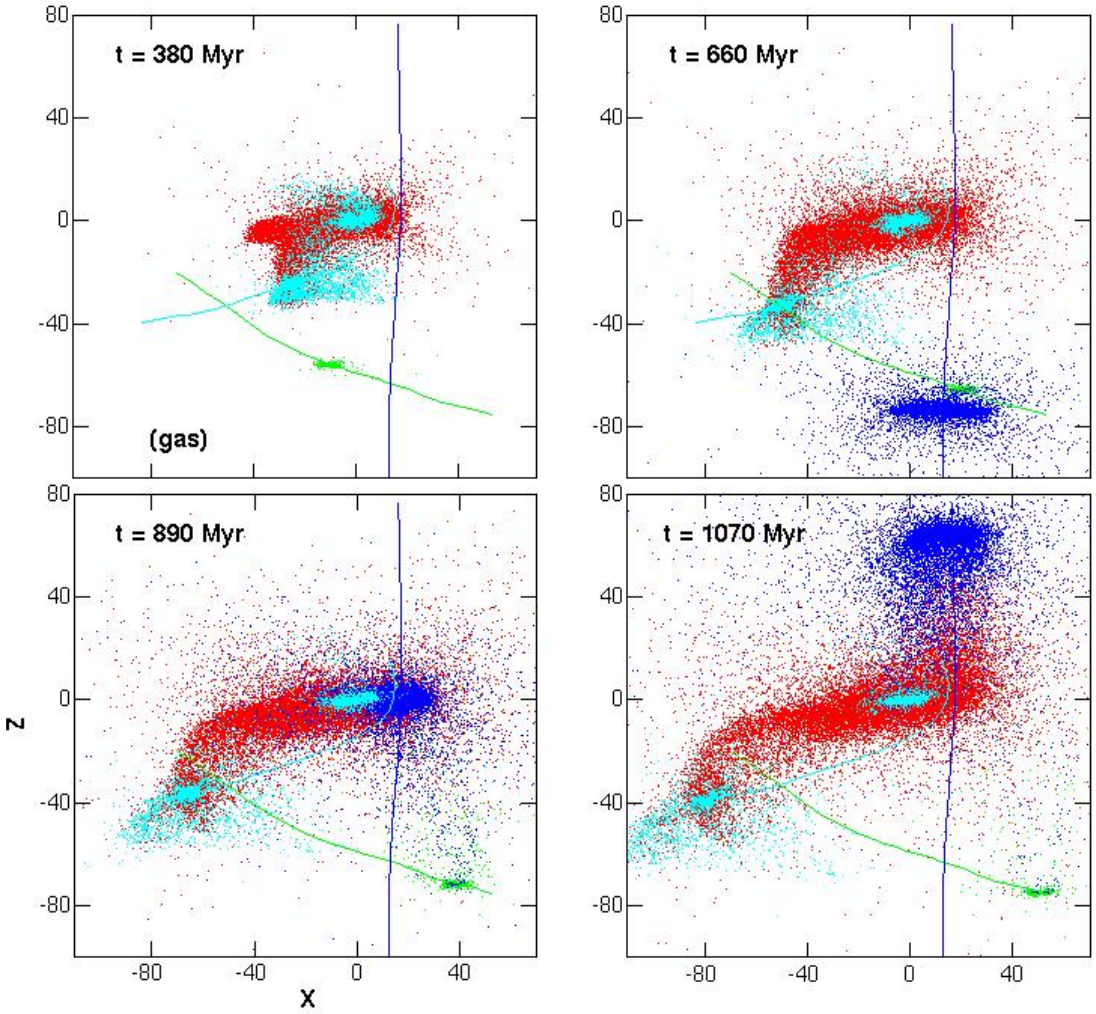

Figure 2.8 Four snapshots from the fiducial model of gas particles projected on to the x-z plane. These are the same snapshots to those in Figure 2.7, showing from the side. (The distribution of star particles at the four times are shown in Figures 2.5 and 2.6.) Colors are used in the same ways in Figures 2.5 through 2.7 (red for G1, green for G2, blue for G3, and cyan for G4). In the top-left panel, G3 is not shown as it is at z $\sim -$ 160.

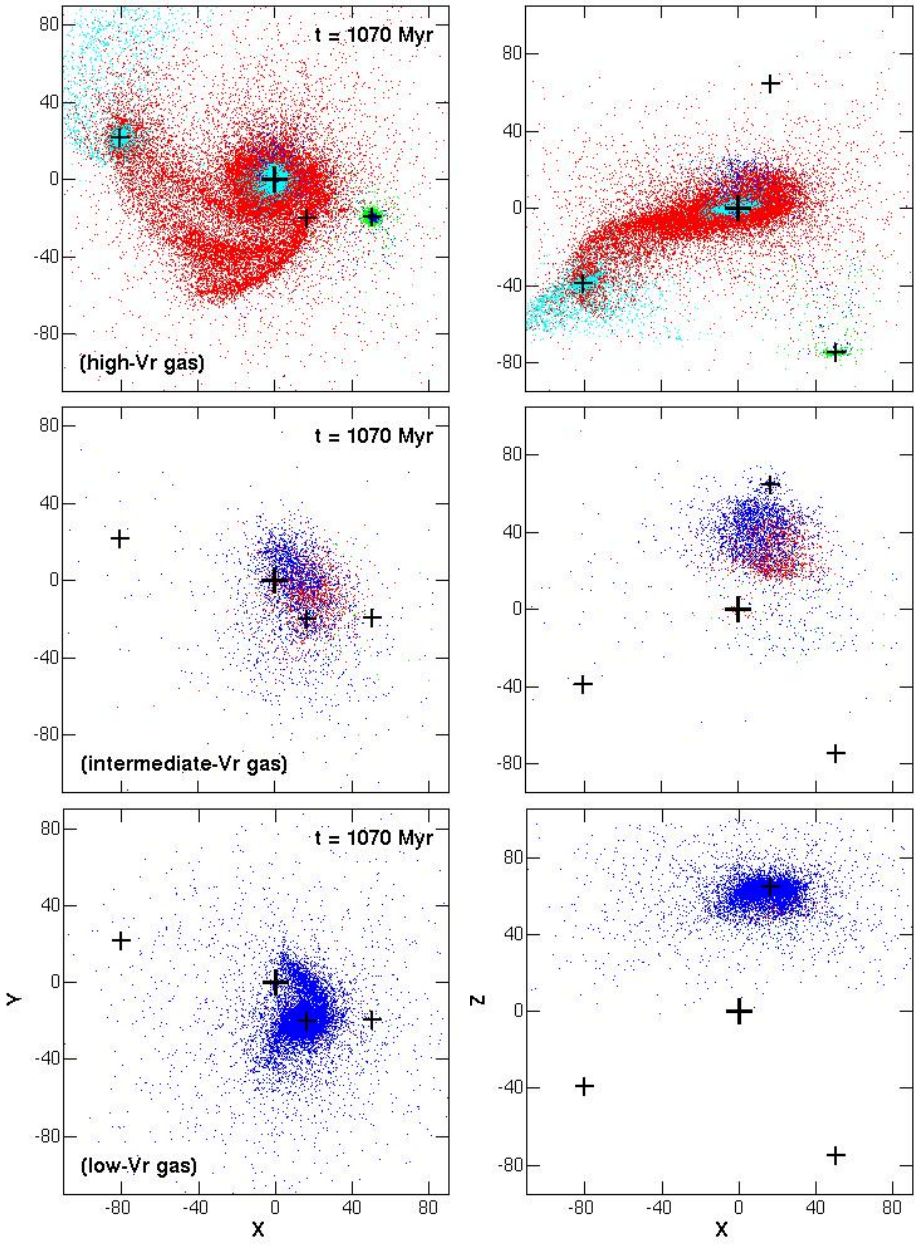

Figure 2.9 Gas particles of the fiducial model at $t = 1070$ Myr in three v_r ranges. (The time is the same to the forth snapshots presented in Figures 2.5 through 2.8.) The top to bottom rows show the gas particles in high, intermediate, and low v_r ranges (see the text how to divide the three ranges). The left and right column show the gas particles projected on to the x-y plane and x-z plane, respectively. Red, green, blue, and cyan dots represent the particles originating from G1, G2, G3, and G4, respectively (red dots are plotted first and then green, blue, and cyan in order). The center positions of the four model galaxies at the instant are indicated with black crosses.

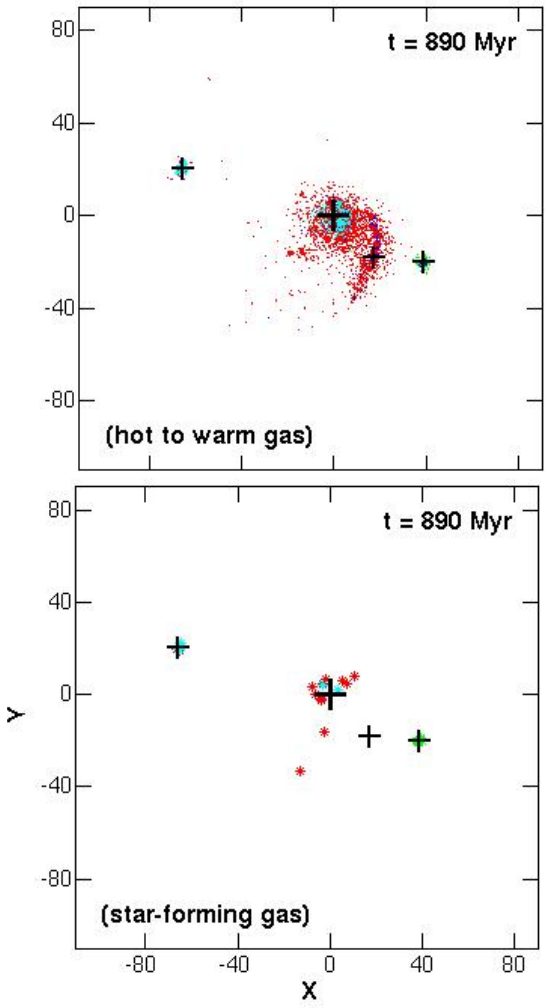

Figure 2.10 Hot to warm gas and star-forming gas particles of the fiducial model at $t = 890$ Myr. (The time is the same to the third snapshots presented in Figures 2.5 through 2.8.) In the top panel, gas particles exceeding a temperature cur off (see the text) and in the high-v_r range are displayed with red, green, blue, and cyan dots (for the particles originating from G1, G2, G3, and G4, respectively). The center positions of the four model galaxies at the instant are marked with black crosses. In the bottom panel, star-forming gas particles in the high-v_r range are shown with small stars in colors.

CHAPTER 3. MODELS OF ARP 285: THE FORMATION OF "BEADS ON A STRING" IN THE ACCRETION TAIL

3.1 Introduction

Galaxy evolution is strongly driven by interactions and mergers between galaxies. Interactions can produce tidal tails and bridges (Toomre & Toomre 1972), increase star-formation rates (Kennicutt et al. 1987; Bushouse et al. 1988), and trigger the formation of young super-star clusters (Holtzman et al. 1992, 1996). Tidal material can contribute to the intergalactic medium (Morris & van den Bergh 1994) and to intergalactic starlight (Feldmeier et al. 2002). Gas-rich galaxy mergers can produce ultra-luminous infrared galaxies (Soifer et al. 1987; Smith et al. 1987; Sanders et al. 1988), while concentrations of stars and gas in tidal features may become independent dwarf galaxies (Barnes & Hernquist 1992; Elmegreen et al. 1993).

The key to understanding these processes is careful comparison of multi-wavelength observations of nearby galaxies with dynamical models. Since interactions and mergers are even more common at high redshift than in the local universe (e.g., Abraham & van den Bergh 2001), detailed studies of nearby interacting systems are important for interpreting high redshift surveys. Such studies can provide information on the timescale of the interaction, the history of gas compression in different regions, star-formation triggering, dissipation in the gas, multiple bursts of star formation, and mass transfer between galaxies (Struck & Smith 2003; Struck et al. 2005; Smith et al. 2005b; Hancock et al. 2007). Computer simulations can provide predictions of the distribution of star formation, which can be compared to observational results to estimate the effects of compression strength, duration, and other factors (e.g., Struck & Smith 2003).

To study star-formation enhancement in pre-merger interacting systems, Smith et al. (2007)

recently obtained mid-infrared observations with the *Spitzer* telescope (Werner et al. 2004) for three dozen interacting galaxies (the "Spirals, Bridges, and Tails" (SB&T) sample) selected from the Arp (1966) Atlas of Peculiar Galaxies. For three of the SB&T systems, Arp 284, Arp 107, and Arp 82, detailed multi-wavelength studies were completed and matching hydrodynamical models of their encounters were constructed: Arp 284 (Smith, Struck, & Pogge 1997; Struck & Smith 2003; Smith et al. 2005a), Arp 107 (Smith et al. 2005b), and Arp 82 (Hancock et al. 2007). A similar study of the interacting pair IC 2163/NGC 2207 was presented by Struck et al. (2005) and Elmegreen et al. (2006), while Arp 24 was studied by Chen & Wu (2007).

In follow-up observations, a multi-wavelength study of another of the SB&T systems, the interacting galaxy pair Arp 285 (NGC 2856/4) was conducted (Smith et al. 2008). As shown in Figure 3.1, this system contains a striking example of "beads on a string": a series of star-formation complexes $\sim$1 kpc apart. These "beads" are found in a tail-like feature extending out perpendicular to the disk of NGC 2856, the more northern galaxy in this widely separated pair. Toomre & Toomre (1972) suggested that this feature is material from the southern galaxy NGC 2854, which has accreted onto NGC 2856 via the bridge. The presence of a massive H I counterpart to this tail and the H I velocity field support this hypothesis (Chengalur et al. 1994, 1995). The *Spitzer* 3.6 μm$-$8.0μm broadband infrared color of the NGC 2856 tail is the reddest of all the tidal features in the SB&T sample (Smith et al. 2007), implying a very young stellar population.

In this study, I have performed numerical modeling of the Arp 285 system, to interpret the observations and particularly to investigate the formation of the tail-like feature, using a smoothed particle hydrodynamics code. I begin in the next section with a review of the major features observed in this system.

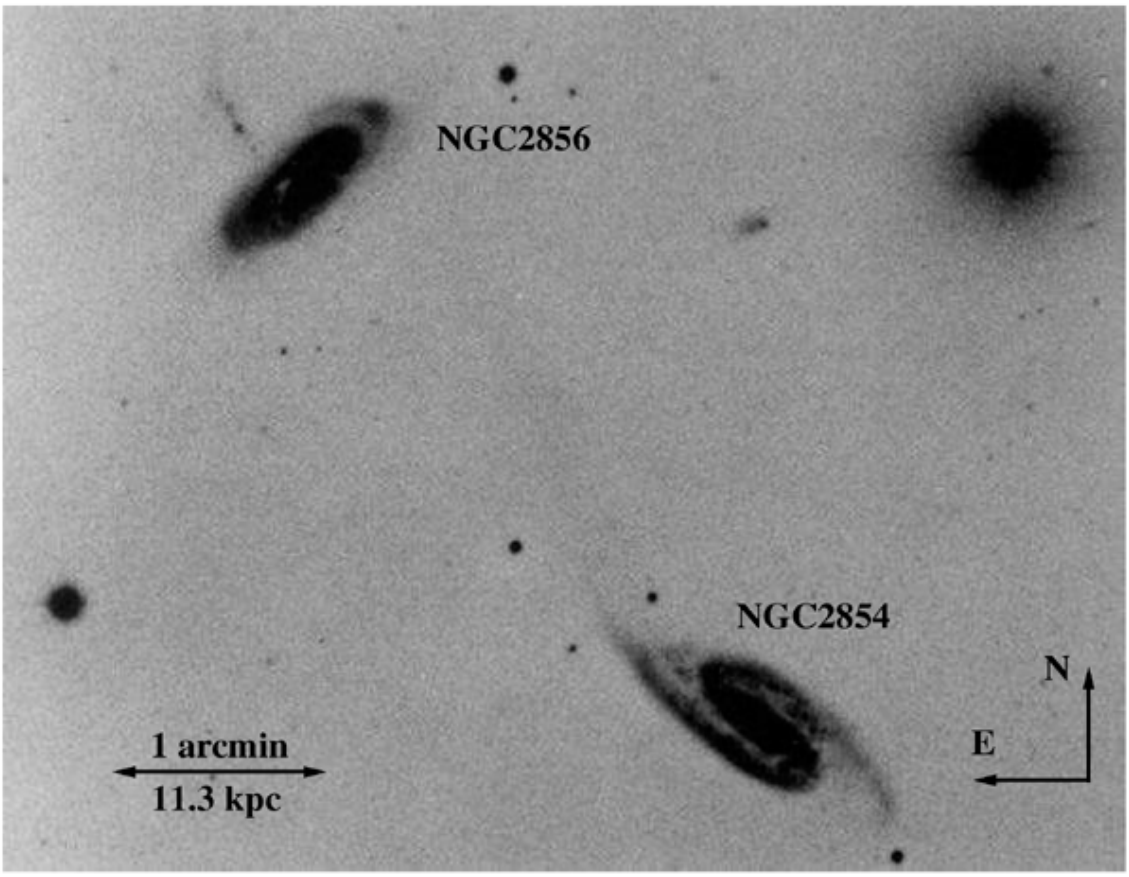

Figure 3.1 The Arp (1966) image of the wide galaxy pair Arp 285 (NGC 2856/4). The northern galaxy NGC 2856 has an unusual "tail" like feature extending out perpendicular to the disk from the middle of the disk. Toomre & Toomre (1972) suggested that this is material from the bridge/companion, which is accreting onto NGC 2856. Note that this tail appears clumpy in this image. Note the "bright spot" in the northwestern edge of the NGC 2856 disk.

3.2 Overview of the Arp 285 system

3.2.1 The morphology of the northern galaxy, NGC 2856

Figure 3.2 presents a montage of multi-waveband images of NGC 2856, the northern galaxy in the Arp 285 pair: *Galaxy Evolution Explorer (GALEX)* far and near-ultraviolet (FUV and NUV) (Martin et al. 2005), Sloan Digitized Sky Survey (SDSS) optical, and *Spitzer* infrared (Smith et al. 2007) images. In the optical images, a dusty spiral pattern and a central bar-like feature are seen in the disk. A series of four clumps are visible along the northern tail in all of the optical images, except for the u image (only two clumps detected) and the z image (only one clump detected). These clumps are labeled on the g image in the last panel in the figure (Smith et al. 2008). From south to north, the separations between the clumps are $7\farcs6$ (1.4 kpc), $6\farcs9$ (1.3 kpc), and $5\farcs1$ (1.0 kpc). Some of the clumps are also detected in the infrared, FUV, and NUV wavebands. In the u through 4.5 μm images of NGC 2856, a "bright spot" is visible in the northwestern edge of the disk of NGC 2856 (see Figure 3.2). This "bright spot" is also visible in the Arp image (Figure 3.1).

In the FUV, NUV, and u images in Figure 3.2, the northeastern portion of the disk is brighter than the southwestern section, but in the longer wavelength images, the disk is more symmetric. This suggests that the difference at shorter wavelengths is due to extinction. This implies that the northeastern side of NGC 2856 is closest to us. This is consistent with the sense of rotation indicated by the H I velocity field (Chengalur et al. 1994), assuming the northwestern spiral arm is trailing.

A connecting bridge between the two galaxies is visible in the smoothed g and r SDSS images (see Figure 3.3), but is not seen in u, i, or z. This bridge is aligned with the "bright spot" in the disk. In Figure 3.3, the northern tail is visible out to $\approx 72''$ (14 kpc) from the disk. A bend and a sudden drop-off in brightness is evident in this tail just north of the four bright clumps of star formation. Another possible faint clump is visible in the smoothed g image $\sim 7.9''$ (1.5 kpc) northwest of clump 4, north of the bend. This bend and the bridge are also visible in the Arp image (Figure 3.1).

3.2.2 The morphology of the southern galaxy, NGC 2854

In Figure 3.4, a montage of the UV, optical, and infrared images of the southern galaxy NGC 2854 is shown. On-going star formation is detected along the spiral arms and at the ends of the bar. The base of the northern tail/bridge appears double in the u, g, r, 5.8 μm, and 8.0 μm images. A series of clumps are visible in the spiral arms in both the optical and the infrared images, and 8 μm-bright sources are seen at the ends of the bar. For some clumps, there are $1'' - 2''$ offsets between the optical and 8 μm peaks; for others, including the nuclear source, there is no clear optical peak associated with the 8 μm source. In the last panel of the figure, eight clumps identified based on the 8 μm image (Smith et al. 2008) are marked.

The southwestern end of the bar is particularly bright in the UV, but less so in the mid-infrared (Figure 3.4). NGC 2854 appears more symmetric in the *Spitzer* images than at shorter wavelengths. This implies that the color variations seen in the optical/UV are due to extinction. The color variations suggest that the southern side of NGC 2854 is the near side, consistent with the H I velocity field of Chengalur et al. (1994) and trailing spiral arms.

The smoothed g image of NGC 2854 is presented in Figure 3.5. A faint optical tail is detected, extending $1\farcm8$ (20 kpc) to the south, coincident with the long H I tail seen by Chengalur et al. (1994). This tail is also visible in the smoothed FUV and NUV images.

Approximately $3'$ due north of NGC 2854, at $9^h24^m2.9^s$, $49°14'41''$ (J2000), a small angular size galaxy is visible on the Arp image (Figure 3.1). This galaxy is detected in all of the *GALEX* and SDSS bands, as well as the *Spitzer* 3.6 μm and 4.5 μm filters. At the present time, no redshift is available for this source, so it is unknown whether it is associated with Arp 285. Its proximity to a very bright star (see Figure 3.1) prevents a reliable Hα detection.

3.2.3 Star-formation properties

Star formation in Arp 285 was investigated using multi-wavelength images (Smith et al. 2008), such as *Spitzer* infrared (Smith et al. 2007), *GALEX* ultraviolet (Martin et al. 2005), SDSS optical (Abazajian et al. 2003), the Southeastern Association for Research in Astronomy (SARA) telescope, and the Two Micron All Sky Survey (2MASS) Atlas near-infrared images

of Arp 285 (Cutri et al., 2006). To estimate the ages of the tail and disk clumps (marked in the last panels of Figures 3.2 and 3.4), Smith et al. (2008) calculated theoretical colors for star-forming regions using version 5.1 of the Starburst99 population synthesis code (Leitherer et al. 1999).

For the series of star-forming regions of the tail ("beads on the string"), very young stellar ages, $\sim 4 - 20$ Myr, were suggested due to the extreme blueness of the optical/UV colors and redness of the mid-infrared colors. Spectral decomposition of these "beads" shows excess emission above their modeled stellar continuum in the 3.6 μm and 4.5 μm bands, indicating either contributions from interstellar matter to these fluxes or a second older stellar population. The "bright spot" in the NGC 2856 disk was estimated to have an intermediate-age stellar population (400−1500 Myr). (For the estimated ages of the other disk clumps and the details of the analysis, see Smith et al. (2008)).

For the tail and disk clumps of Arp 285, Smith et al. (2008) also provided the range of stellar masses inferred from their Starburst99 models and compared to stellar masses of various other objects. It was estimated that the tail clumps are similar in mass to Galactic globular clusters, but have lower stellar masses than those inferred for TDGs and dwarf irregular galaxies; the mass of the NGC 2856 disk "bright spot" is near the median for dwarf irregular galaxies.

3.3 Numerical model of the encounter

To interpret the observational results in terms of the dynamical and star forming history of Arp 285, I have constructed a numerical simulation of the Arp 285 interaction using the smoothed particle hydrodynamics (SPH) code of Struck (1997). (This code (or a modified version of the code) was also used to model SQ and to study slowly developing spiral waves which are presented in chapter 2 and 4, respectively.)

3.3.1 Constraints on the Model

Arp 285 is less symmetric than the ring galaxies or planar fly-by encounters such as M51, NGC 2207/IC2163, and Arp 82. The collisional morphology of Arp 285 appears somewhat

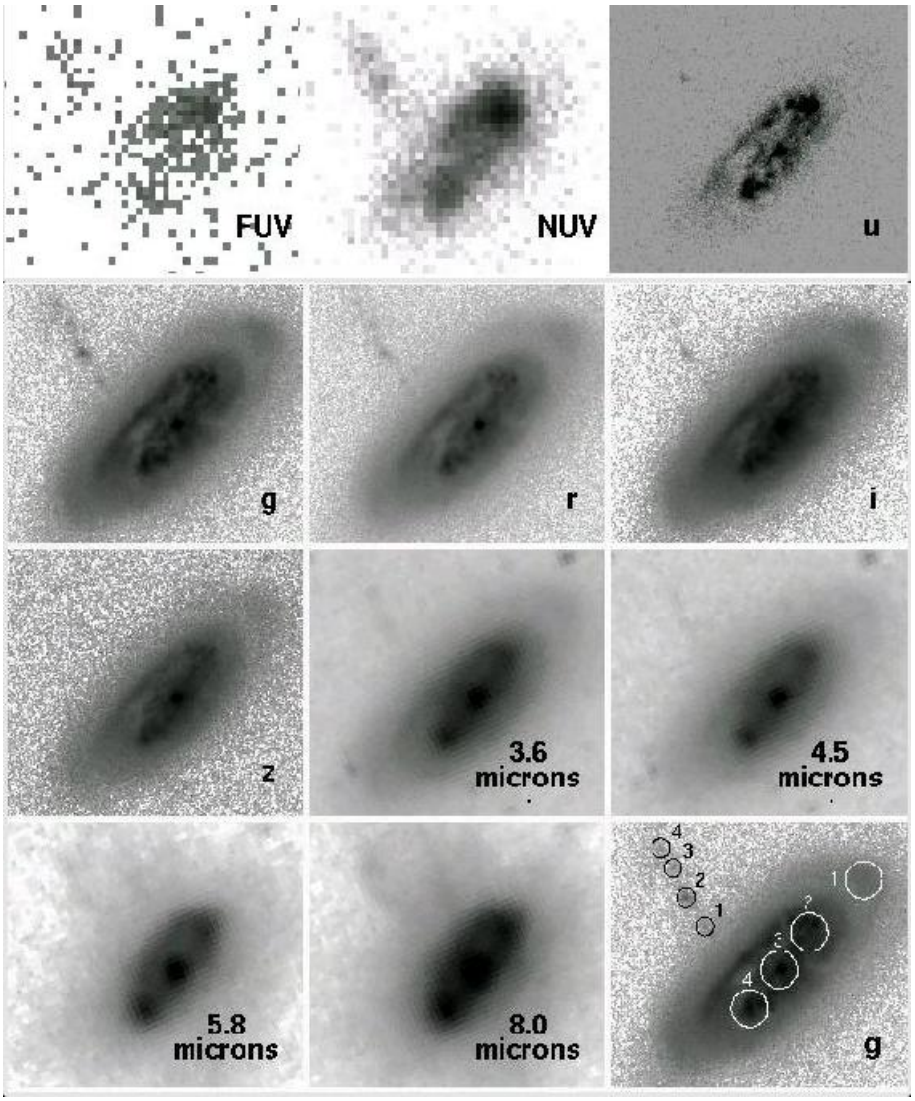

Figure 3.2 A montage of the *GALEX*, SDSS, and *Spitzer* images of NGC 2856, the northern galaxy in Arp 285 (Smith et al. 2008). North is up and east to the left. The field of view is $1\farcm1 \times 0\farcm9$. Notice the series of clumps in the northern tail. The tail clumps are enclosed by $1\farcs61$ black circles in the last panel on the g image. The NGC 2856 disk clumps are marked in the last panel by $4''$ radius white circles. Disk clump 1 is the "bright spot" mentioned in Section 3.2.1.

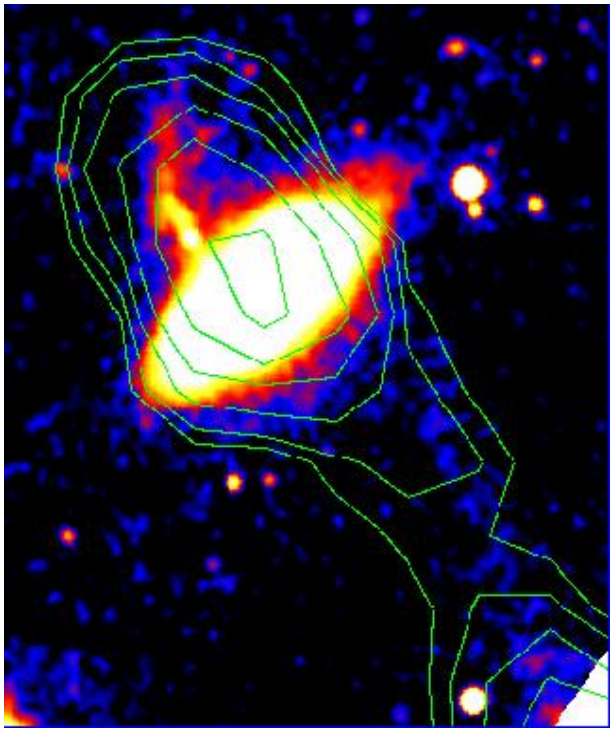

Figure 3.3 The smoothed SDSS g image of NGC 2856 (color; Smith et al. 2008), with 21 cm H I contours (from Chengalur et al. 1994) superimposed. North is up and east to the left. Notice the bridge connecting this galaxy to its southern companion NGC 2854. Also note the bend in the northern tail north of the clumps marked in Figure 3.2. The field of view is $3\farcm0\times3\farcm3$. The H I beamsize is $29''\times29''$, and the H I contours are (2.6, 4.6, 8.1, 14, 25, 43, and 76) $\times10^{20}$ cm^{-2}.

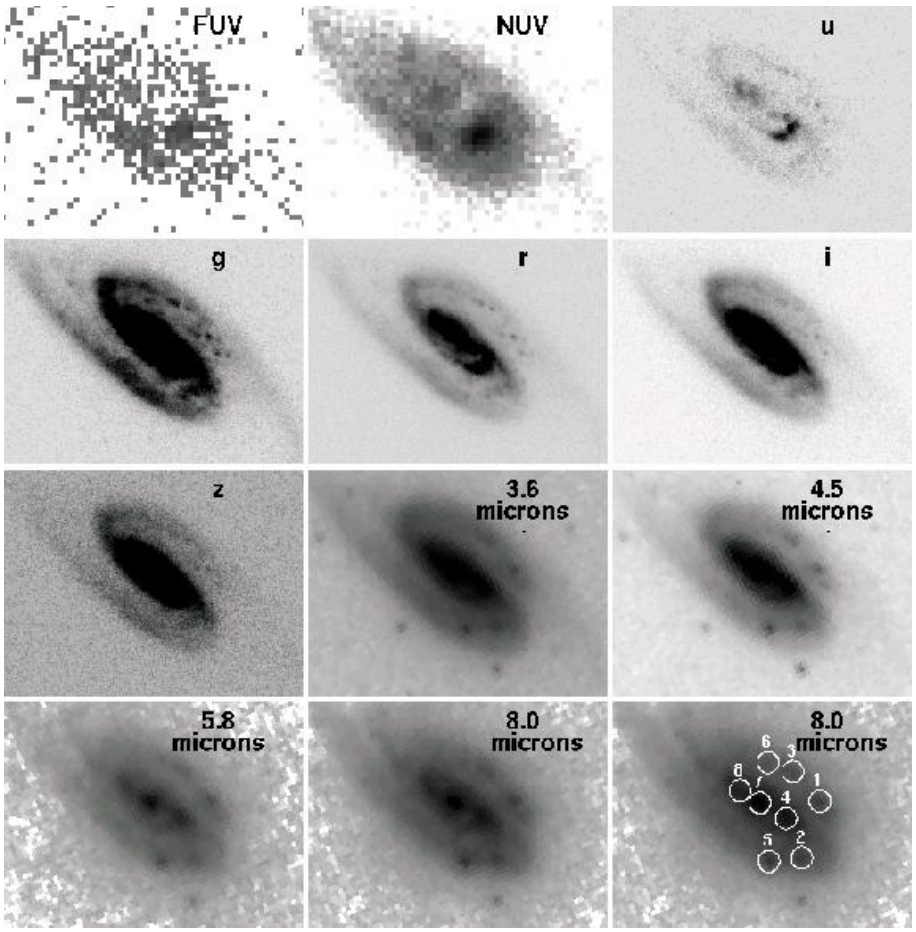

Figure 3.4 A montage of images of the southern galaxy in Arp 285, NGC 2854 (Smith et al. 2008). North is up and east to the left. The field of view is $1\farcm2 \times 1\farcm0$. Notice the series of clumps in the northern spiral arm. In the UV and optical, the southern end of the bar is brighter than the northern end. At longer wavelengths, the disk is more symmetrical. The 8 μm-selected clumps are circled on the 8 μm image in the last panel. The circles have $2\farcs8$ radii.

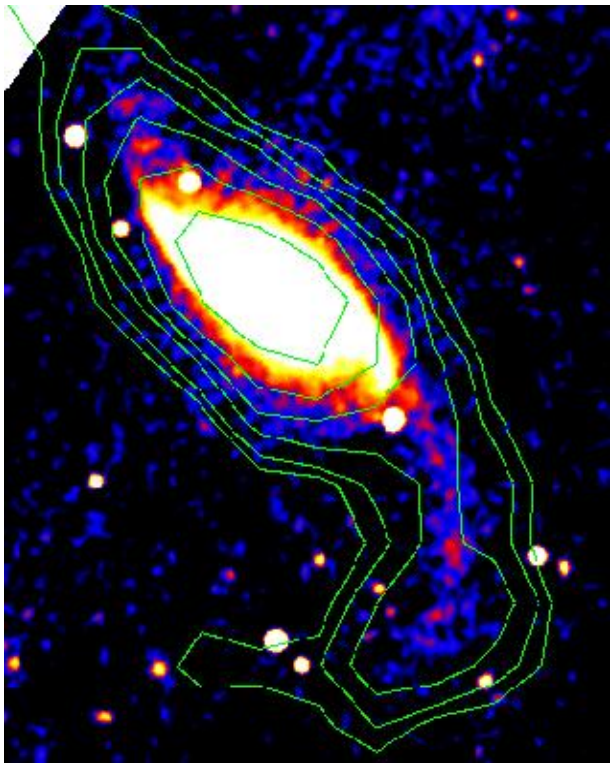

Figure 3.5 The smoothed g image of NGC 2854 (Smith et al. 2008) with 21 cm H I contours (Chengalur et al. 1994) superimposed. North is up and east to the left. The field of view is $3\farcm4 \times 4\farcm2$. Note the long tidal tail extending $1\farcm8$ to the south. The H I beamsize is $29'' \times 29''$, and the H I contours are (2.6, 4.6, 8.1, 14, 25, 43, and 76) $\times 10^{20}$ cm^{-2}.

similar to that of Arp 284, an asymmetric ring/tail galaxy (NGC 7714) with an edge-on companion (NGC 7715). The substantial bridge and tail of NGC 2854, like those of NGC 7715, suggest that it suffered a strong prograde encounter. There are also similarities between NGC 7714 and NGC 2856. The optical images show that the "bright spot" in the northwestern section of the NGC 2856 disk (disk clump 1) is part of an arc-like structure (see Figures 3.1 and 3.2). This arc is reminiscent of the partial ring in NGC 7714 (see the Arp (1966) photograph of Arp 284), which has been successfully modeled by an off-center collision (Struck & Smith 2003). It is also reminiscent of the "ripples" in Arp 227, which were also modeled by a ring galaxy-like collision by Wallin & Struck-Marcell (1988).

There are some differences between NGC 2856 and NGC 7714, however. In contrast to NGC 7714, NGC 2856 lacks strong tidal tails, except for the northern tail perpendicular to the disk and a short H I extension to the northwest (Chengalur et al. 1994). This suggests that NGC 2856 did not experience the encounter as very prograde. It also does not have the fan-like form common to strong retrograde encounters. This suggests that the orbital path of the two galaxies is at a large angle to the plane of the NGC 2856 disk.

These considerations provide some idea of the type of collision that produced the current morphologies. In the simulation of this encounter, I have limited myself to the goal of reproducing the large-scale morphological structures, but have not attempted to simulate internal disk structures nor match the system kinematics in any detail.

One key feature I would like the models to help us understand is the beads in the tail north of NGC 2856. Several conceptual ideas for the origin of this material have been considered in this numerical study. The H I morphology suggests that this material is an extension of the bridge from NGC 2854, though the optical observations look as though the bridge curves away from that direction before connecting to the bead region. It may be that the bridge is in fact a tidal tail, which is merely projected onto NGC 2856, not connected. However, the H I kinematics indicate that this is unlikely. Moreover, the bead material seems strongly affected by the gravitational potential of NGC 2856.

Thus, it seems likely that the bead material is accreting onto the halo of NGC 2856 from

the bridge. There are two possibilities for how this occurs: (i) as infall through the disk of NGC 2856 and out the other side, or (ii) by swinging around that disk to the other side. It is difficult to distinguish between these two scenarios observationally. In option (i) it can be imagined that clouds pushing through the NGC 2856 disk are shocked and compressed. This may trigger star cluster formation, accounting for the beads. I would naively expect this process might be sequential, so that the beads furthest from the disk are oldest. In contrast, in option (ii), a group of inflowing clouds pile up in the halo of NGC 2856 and collide with the material that arrived earlier. This could trigger star formation simultaneously at several locations. Thus option (i) would predict an age gradient, while for option (ii) roughly coeval clumps would be expected. With the available data, I cannot distinguish between these two possibilities, since the expected age gradient for option (i) is too small to measure. Assuming a nominal velocity for the tidal material away from the disk of $\sim$300 km s^1 and motion in the plane of the sky, for scenario (i) it would be expected that an age difference of $\sim$12 Myr between the first and fourth clumps in the tail, and $\sim$4 Myr between clumps 2 and 3. This is smaller than the uncertainties on the ages of these clumps (Smith et al. 2008).

Another way to distinguish between these two scenarios is with numerical models of the interaction. For option (i), I was not able to construct a viable simulation with a small number of trial runs. The fundamental difficulty is that in order to produce the spirals and other tidal structures in NGC 2854 the collision must have a substantial prograde fly-by component with respect to NGC 2854. In that case, however, material accreted onto NGC 2856 from NGC 2854 generally has too much relative angular momentum to fall directly onto the NGC 2856 disk. Because of this, I suspect that such models occupy a small volume of the collision parameter space. I have therefore chosen to focus on models for option (ii). These are discussed in the next two sections.

3.3.2 Model details

In the SPH code, hydrodynamical forces are calculated on a grid with fixed spacing. Gravitational forces are computed between particles in adjacent cells, to capture local gravitational

instabilities. The model galaxies have disks containing both gas particles and collisionless star particles, as well as rigid dark halo potentials (see Struck 1997 for details). Gas particles with densities exceeding a constant density threshold are identified as star-forming particles. These generally exceed the local Jeans critical mass. A number of simulations were run; I will only present the results of the best model.

The evolution of the numerical model for the Arp 285 system is presented in Figure 3.6. I adopt the convention that the model primary corresponds to the southern galaxy NGC 2854 and the companion to NGC 2856. The particles in Figure 3.6 are color coded according to their galaxy of origin, with red particles originating from the primary disk and green from the companion. A total of 13,590 star and 42,900 gas particles were used in the primary disk and 5,640 star and 5,640 gas particles in the secondary disk. In this model, the length unit = 1.0 kpc, and the time unit is 200 Myr. Figure 3.6 shows four time steps in the simulation. The first plot (top left) shows the appearance in the plane of the sky near the time of closest approach, where the separation between the two galaxies is ∼12 kpc. The second plot (top right) shows the system 370 Myr after closest approach, while the third (bottom left) shows its appearance 510 Myr after closest approach. These two plots match approximately the observed appearance at the present time. The last plot shows the appearance 740 Myr after closest approach, the predicted appearance in the future.

The radii of the primary star and gas disks are 6.0 and 10.8 kpc, respectively. The companion star and gas disk radii are both 3.6 kpc. The primary disk was set up in the x-y plane. The companion disk is first set up in the x-y plane, then rotated 40° around the y-axis through its center, and then 90° around the z-axis passing through its center. The relative orbit of the companion is in the x-y plane, so from the point of view of the companion disk, the primary approaches at a fairly steep angle. In the companion disk of the model in Figure 3.6, the south side is the near side.

The orbit is counter-clockwise, as is the rotation of the primary, so it sees the encounter as very prograde. The companion disk rotation, in the x-y plane before the tilts are applied, is clockwise. The initial (x, y, z) position of the companion relative to the primary center is

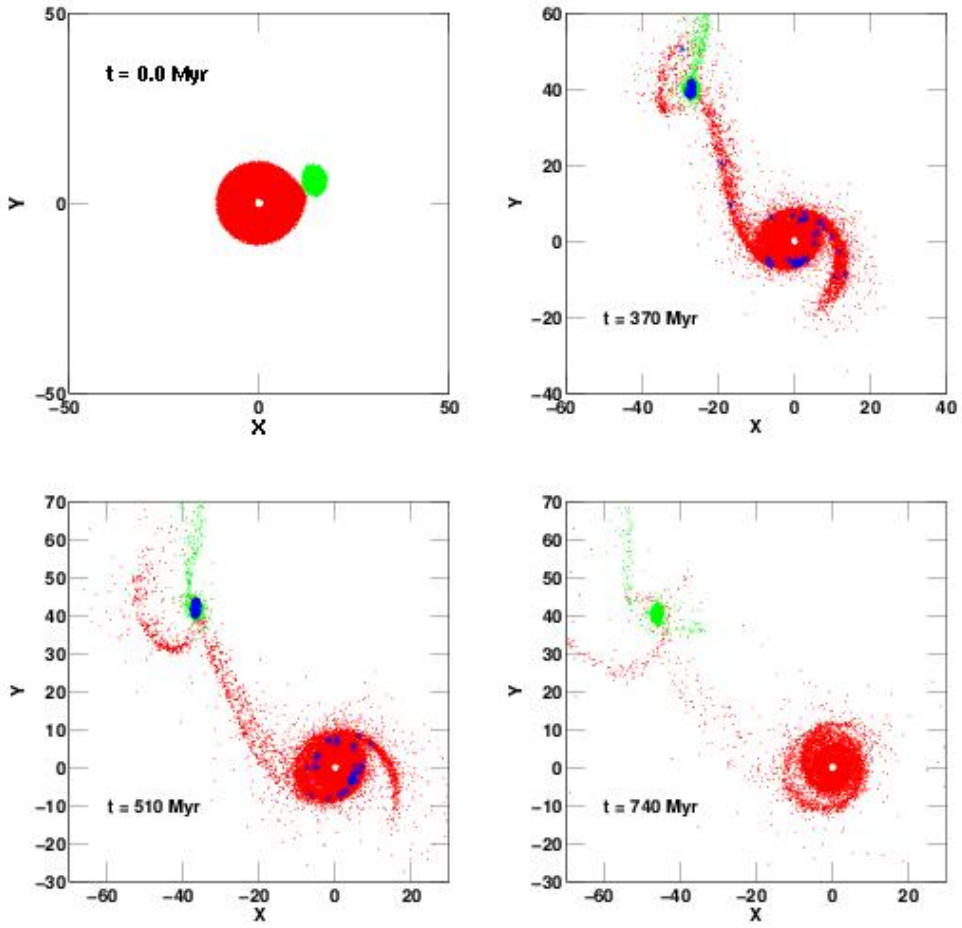

Figure 3.6 Snapshots of the model gas disks. The stellar appearance is similar. Red particles originated in the primary galaxy, green in the companion. The top-left panel shows a time near closest approach ($T = 0$ Myr). The companion has swung in from the lower left, and swings around to an apogalacticon point at later times. The upper-right panel and the lower left are at times near the present ($T = 370$ Myr and 510 Myr, respectively). The lower-right panel is at a later time ($T = 740$ Myr), when the companion begins to fall back to merge with the primary. In the first three panels every third gas particle is plotted with a dot. In the second and third panels blue asterisks mark star-forming particles, except those within 5 kpc of the primary center, which were omitted for clarity. The star-forming region in the northern tail was produced from gas accreted from the companion, while the star-forming regions in the central region of the northern galaxy were produced from gas that originated in the northern galaxy. The star-forming regions in the bridge, southern galaxy, and southern tail were formed from gas that originated in the southern galaxy. In the final panel only every fifth particle was plotted, to show the persistent spiral in the primary disk. The motion of the companion around the point of greatest separation is very slow, so little positional change is evident in the last three panels.

(−8.9, −20.0, 0.0) kpc. Its initial relative velocity is (250, 75, 0) km s^{-1}.

The form of the halo potential of the two galaxies is such that the acceleration of a test particle in this halo is

$$a = \frac{GM_h}{\epsilon^2} \frac{r/\epsilon}{(1 + r^2/\epsilon^2)^{n_h}}, \tag{3.1}$$

where M_h is a halo mass scale, ϵ is a core radius (set to 2.0 and 4.0 kpc for the primary and companion, respectively), and the index n_h specifies the compactness of the halo. For the primary I use $M_h = 1.3 \times 10^{10} M_\odot$ and $n_h = 1.2$, which gives a slightly declining rotation curve at large radii. For the companion I take $M_h = 2.8 \times 10^{10} M_\odot$ and $n_h = 1.35$, which gives a more rapidly declining rotation curve. The model includes the effects of dynamical friction with a Chandrasekhar-like frictional term (see Struck & Smith 2003). The effects of this term are small except near the closest approach.

With these potentials, the halo masses for the primary and companion out to a radius of 12 kpc (about the separation at closest approach) are $3.7 \times 10^{10} M_\odot$ and $3.4 \times 10^{10} M_\odot$, respectively, with a ratio of about 0.92. This is in accord with the near equality of the r and i band luminosities of the two galaxies (Smith et al. 2008).

3.3.3 Model results

The general morphology of the system is quite well reproduced by the model, including the moderate countertail on NGC 2854 and the bridge (see Figure 3.6). A very close encounter is required to produce a bridge as massive as observed. On the other hand, the moderate-sized tail of the primary galaxy is the result of a prograde perturbation that was not prolonged. These facts, and the relatively large separation between the galaxies, argue that the relative orbit of the companion is quite elliptical, as in the model.

The model primary disk is more circular in appearance than that of NGC 2854. There are several possible reasons for the difference. The first is simply that the model disk should have a greater tilt relative to the plane of observation (here the x-y plane). The primary disk in the model is in the x-y plane of the sky. However, as noted in Section 3.2.2, based on extinction arguments and the H I velocity field, the real disk is somewhat inclined to the line of sight,

with the south side closest. It is also possible that tidal stretching is responsible for the shape of the primary disk. However, in that case I might expect a longer and more massive tidal tail. This is a rather soft argument at present, but it does appear that the bar and the spiral arms of the primary disk are disproportionately strong relative to the tail. This suggests that the bar and spiral arms were present in the NGC 2854 disk before the encounter. This possibility was not included in the modeling.

In addition to the bridge, the model companion galaxy has two tidal tails, one made of material originating from the companion galaxy itself, and the other from material accreted from the primary galaxy along the bridg (see Figure 3.6). The tidal plume drawn off the companion disk is visible as the green feature extending northward in the last three panels of Figure 3.6. I equate this structure with the H I emission extending to the northwest in the Chengalur et al. (1994) H I maps, though it is not at the same position angle as in the observations, being oriented about 45° too much to the north compared to the data. The red feature extending to the northeast in Figure 3.6 I associate with the northern H I tail containing the "beads" of star formation. As with the other feature, the position angle of the model tail is somewhat off from the observed orientation.

In the model, the disk of the companion was tilted relative to the direction of the encounter, so the perturbation had both an orthogonal, ring-galaxy-like component, and a retrograde component. Waves with circular arc-like components develop in the disk of the companion. This behavior might account for the northwest arc-like structure in NGC 2856 containing the "bright spot."

As with NGC 2854, the observed structure of NGC 2856 also shows a bar and internal arms. However, in this galaxy the structure of the bar is rather irregular. The simulation shows that a large mass of gas loses angular momentum as a result of the encounter, and forms a compressed inner disk or bar. Thus, the bar in NGC 2856 may be the result of the collision, and may not have existed before the encounter.

The evolution of the bridge in this model is especially interesting. Because of its elliptical trajectory, the companion speeds past its point of closest approach as the bridge begins to

form. As the bridge initially stretches outward from the primary center, it lags behind the companion. Later, the companion nears its apogalacticon relative to the primary, and slows, so that the bridge catches up to it. The bridge material has a significant angular momentum relative to the companion center, so that the outermost points swing around to the far side of the companion. Shortly thereafter the bridge material begins to pile up at an outer radius northeast of the companion. As time goes on, more bridge material streams into this pile-up region, and compression drives star formation. In Figure 3.6, star-forming gas particles are marked with cyan asterisks. In the second panel, one asterisk is visible in the pile-up region. Comparison of different time steps and different models shows that the star formation there is quite stochastic. Sometimes there are a number of star-forming particles there, and occasionally they line up like the observed "beads". Since the model does not accurately represent the effects of self-gravity across this pile-up region, the real environment may trigger more such star formation than in the model.

Material from both the accretion tail and the companion's plume eventually accrete onto the companion. Gas in the companion is compressed by the tidal perturbation, and experiences prolonged accretion. In the model, the density threshold for star formation is easily exceeded, and central star formation continues for some time. This is consistent with the uncertainties on the age of the stellar population in disk clump 3 (the nucleus) of NGC 2856 (Smith et al. 2008).

This simulation somewhat resembles models of polar ring formation via accretion from a companion (Reshetnikov et al. 2006), however, the two model galaxies merge before this polar ring proceeds very far in its development. The star clusters formed in the pile-up region will eventually be carried with the companion halo into the merger with the primary. They are likely to end up orbiting in the inner halo of the merger remnant and possibly adding to the globular cluster population there. This is in contrast to dwarf galaxies formed at the end of tidal tails, which may spend long periods in the outer halo.

3.4 Discussion and summary

The clumps in the northern tail of NGC 2856 are a striking example of the "beads on a string" phenomenon, in which star-forming regions are regularly spaced ∼1 kpc apart along spiral arms and in tidal features (Elmegreen & Efremov 1996). This numerical model of the Arp 285 system aimed primarily to study the formation of those "beads" and to compare with the recent observational study of the system (i.e., Smith et al. 2008).

The optical-UV colors of the "beads" are very blue, and imply ages of only ∼4-20 Myr (Smith et al. 2008), which is much younger than the time since the point of closest approach between the two galaxies, showing that there is a time delay between the initiation of star formation and the time of closest approach between the two galaxies. This numerical model of the system shows that there should be an underlying older stellar component in this tail, made of stars stripped from the NGC 2854 disk. Diffuse optical light is clearly present between the clumps, and the stellar tail extends 41″ (7.8 kpc) to the north beyond clump 4.

In this numerical model, gas from the bridge falling into the potential of the companion overshoots the companion, piling up in an accretion tail on the far side of the companion. Star formation occurs in this region. The model suggests that the "beads on the string" may be the result of stochastic processes, albeit in a density enhanced pileup zone. It is possible that local self-gravity is pulling clumps together. The spacing between the star-forming regions in the model is comparable to the scale of local self-gravity in the code. At most time steps, the star formation is found in a couple of isolated clumps, without any "bead" appearance. Thus it appears we see this feature at a favorable time.

This model also suggests that the so-called "bright spot" in the northwestern portion of the NGC 2856 disk, and its associated arc, were likely to be caused by a ring-like perturbation of the disk by an encounter which was mainly perpendicular to the plane of the NGC 2856 disk. The age of the stellar population in this region was estimated to be between 400 and 1500 Myr (Smith et al. 2008), while the interaction model indicates that the point of closest approach between the galaxies occurred between about 300 and 500 Myr ago. This is consistent with the idea that the brightness of this "spot" may be due to the past star formation triggered by

the encounter.

CHAPTER 4. MODELS OF SPIRAL WAVES PRODUCED IN FAST GALAXY COLLISIONS

4.1 Introduction: a surprising simulaion

Fast collisions between galaxies have been little studied. Perturbations of short duration have much less effect than those between comparable galaxies with greater persistence, e.g., see the reviews of Struck (1999) and Struck (2006). Exceptions to this generalization include direct collisions at high speed, where proximity offsets brevity, and cases where multiple fast, weak disturbances in a cluster environment might have a cumulative effect, the so-called harassment effect (Moore et al. 1996). Certainly in fast collisions with unbound or marginally bound partners there has been little motivation to look for long-term effects.

In this study, numerical simulations of such interactions have been undertaken and compared to semi-analytic models based on the impulse approximation like those published by Gerber & Lamb (1994, also Sundelius et al. 1987, Struck-Marcell 1990) with the hope to extend the results of the earlier studies in several directions. The model results, such as those shown in Figure 4.1, provided several surprises (Struck et al. 2010). Specically, Figure 4.1 shows the evolution of waves in the model disk stars, with time measured in code units from the time of closest approach between the two galaxies. The code time unit equals about 0.8 of the orbital time of a star at the outer edge of the disk (see Section 4.2).

The early response of the disk is very mild, as expected. The first surprise is that the spirals do not dissipate in a few (outer disk) orbital times. The rapid disappearance of spiral waves by wind up and dissipation has been a problem since the earliest development of the theory, see discussion in Binney & Tremaine (2008). Over the years there have been various suggestions about how this fate might be avoided. These include the stabilizing effects of

gaseous dissipation, e.g., Chakrabarti (2008, and references therein), and the offset between the extrema of the density and gravitational potential in a wave (Zhang 1998). The figures from the simulations suggest that, in fact, the ameliorating effects of these processes are not very effective. On the contrary, Sellwood (2010) has suggested that spirals are transient, but that they continuously regenerate via a recurring cycle of instability.

In Figure 4.1 the density contrasts across the spiral density waves grow stronger for a time, and the waves do not wind up at a particular (e.g., resonant) radius. This growth is not as rapid as in the case of swing amplication in disks with low values of the Toomre (1981) Q parameter. The dimensionless Toomre parameter $Q = \kappa\,\sigma/(3.36\,G\,\Sigma)$ for stars, with surface density Σ, epicyclic frequency κ, and velocity dispersion σ, implies local gravitational instability at values less than about 1.0 (see Binney & Tremaine 2008). The waves are greatly stretched due to the shear in the disk. This is expected from classical density wave theory (Binney & Tremaine 2008, and references therein), and as seen in many other simulations, which generally have stronger initial wave amplitudes. The second surprise is that the after this initial wave steepening, or breaking, the waves continue to persist for a much longer time (more than 10 outer orbital periods in the model of Figure 4.1) while winding ever tighter. A number of checks were made to eliminate the possibility of numerical errors in the code or graphical errors. It will be seen below that the results can be accounted for with analytical calculations.

The case shown in Figure 4.1 is a planar flyby, which is prograde as seen by the model disk. From a number of other cases run to date it appears that for fast flyby collisions the amplitude of the disturbance matters more than other details of the encounter orbit. For example, it is also possible to generate similar (trailing) waves after a retrograde encounter, but since the flyby is effectively shorter (as seen by disk stars) than the corresponding prograde collision the disturbance is weaker. The evolution of a gas disk was included in some of our models. The waves in the gas disk are quite weak, in contrast to the stars in Figure 4.1. This and limited particle resolution in the present models prevent us from resolving gas pulled into the potential wells of the stellar waves.

4.2 Description of the numerical models

The basic code used to produce the simulation of Figure 4.1 was that of Struck (1997). This is an SPH gas dynamics code, but the hydrodynamics does not play a signicant role in the present study. A simple leapfrog integrator is used to advance the stellar orbits. The gravitational potential of each galaxy is modeled with fixed, rigid halo potentials of the softened power-law form described in earlier chapters (see Equation 2.1 or 3.1). Specifically, the potential of the model disk is such that its rotation curve is linearly rising in the core, and flat at radii much larger than the softening length of one unit. The potential of the companion is of the same form, except moderately declining at large radii.

Forces are computed on a fixed grid for computational simplicity, and local self-gravity is computed between particles in adjacent grid cells. Because of the disk shear it is negligible on much larger scales. The grid size is 0.05 code units. The code length and time units are scaled to 2 kpc and 333 Myr in this work. Then the outer orbital period of about 0.8 units equals 270 Myr. A total of 38,100 particles were used to model the primary star disk, whose initial size was about 9.0 kpc in the adopted units. The flat rotation curve velocity of the disk was 220 km s^{-1}, derived from a scale mass of $2.2 \times 10^{10} M_{\odot}$ within a radius of 2.0 kpc. The companion consisted of a halo potential only.

The companions mass was taken to be about twice that of the target galaxy. The initial position of the companion was about 120 kpc south of the primary with initial velocity components of 150 km s^{-1} west (toward positive x values), and 600 km s^{-1} northward. The relatively high value of the companion mass was given to achieve a signicant perturbation at the distance of closest approach, which was about 2.6 times the size of the initial disk, and the high flyby velocity. The companion orbit was only perturbed by an angle of about 20° in the encounter.

4.3 Explanations from Analytic Models

To understand the results of the numerical simulations, the numerical model is compared with a semi-analytic model (Struck et al. 2010), in which the orbits of stars initialized on a

disk-covering grid were analytically calculated. In the analytic model, assuming a perfectly flat rotation curve for simplicity, each star was initially assigned an azimuthal velocity equal to the circular velocity, and zero radial velocity. In the Impulse Approximation it is assumed that in the encounter each star experiences an acceleration a in the direction of the companion for a short time interval Δt. In the analytic model, it is assumed that the acceleration equals the classical, textbook tidal acceleration, which is also the small amplitude limit of more complete expressions (see e.g., Gerber & Lamb 1994). Specifically, the following velocity component impulses are added to the velocities of each star:

$$\Delta v_r = \Delta V \frac{r}{D} cos(2\phi), \;\; \Delta v_\phi = \Delta V \frac{r}{D} sin(2\phi), \tag{4.1}$$

where (r, ϕ) are the radial and azimuthal positions of the star, D is the total size of the disk, and ΔV is a constant velocity amplitude factor that includes the usual tidal constants and the ratio of the disk size to the distance of closest approach.

The epicyclic approximation is used in the analytic model to compute the stellar orbits. Specically, the orbit equations are,

$$\begin{aligned} r(t) &= q - Aqsin(\kappa t + \psi), \\ \phi(t) &= \phi_o + \omega_{cir}(q)t + \sqrt{2}A\{cos(\kappa t + \psi) - cos(\psi)\}, \end{aligned} \tag{4.2}$$

where (q, ϕ_o) are the initial values of (r, ϕ), κ is the epicyclic frequency, ω_{cir} is the circular frequency, ψ is the epicyclic phase after the impulse, and A is the epicyclic amplitude. Note that because of the angular momentum change resulting from the azimuthal velocity impulse, the radius of the guiding center circle (i.e., of the epicycle's center) does not equal the star's initial radius. In Equation 4.2, q equals the former not the initial stellar radius, and all of the quantities: κ, ψ, ω_{cir}, and A are computed with this q. The values of ψ and A in terms of ΔV and the initial positions are derived by comparing the epicyclic velocities derived from Equation 4.2 to those of Equation 4.1.

Figure 4.2 shows an example of stellar disk evolution according to this prescription, with the choice $\Delta V = 0.1$. The figure shows snapshots at three times, as described in the caption, with the final panel, in the lower right showing a snapshot of the numerical model for comparison

with the analytic model. In order to make the comparison two adjustments were made to the analytic model disk (Struck et al. 2010). First, it was rotated by 90° to better match the point of closest approach in the numerical model. Secondly, the time was adjusted by subtracting an interval of 0.45 units. The reason for this offset is that the velocity impulse is applied instantaneously in the analytic case, but is not realized in the numerical model until the companion is well past closest approach.

Granted these adjustments, the comparison in the bottom row of Figure 4.2 is very good. Comparisons between the panels in the top row and the corresponding timesteps in Figure 4.1 are also good. The most obvious difference is that the spirals are discernable to very small radii in the analytic, but not the numerical model. Experimentation shows that this is a function of the amplitude A in the analytic model, but no attempt has been made to optimize that fit. It is also the result of different halo potentials in the central regions. The numerical model has a rising potential in the inner half of the disk, not a flat one like the analytic model. The curve drawn over one of the two waves in the later two analytic figures and transposed from the last onto the numerical model, fits in the outermost parts, but diverges in the inner.

The agreement between numerical and analytic waves indicates that the former is not a numerical artifact. It also confirms that these are kinematic waves. The question is - why do they not dissipate more rapidly as they wind up? In the context of density wave theory it is expected that as the waves shear their amplitude will decrease, unless conditions are right for swing amplication. However, these waves are not produced by a local disturbance that simply stretches away. They are the result of a globally correlated initial disturbance. That statement also applies to the original swing amplier simulations too (see Toomre 1981), but self-gravity was relatively strong in these disks (Toomre factor of Q = 1.5), while the present models have a large value of Q (or negligible 1/Q, because a low value has been assigned to the particle mass). (For more discussion on the analytic model, see Struck et al. 2010.)

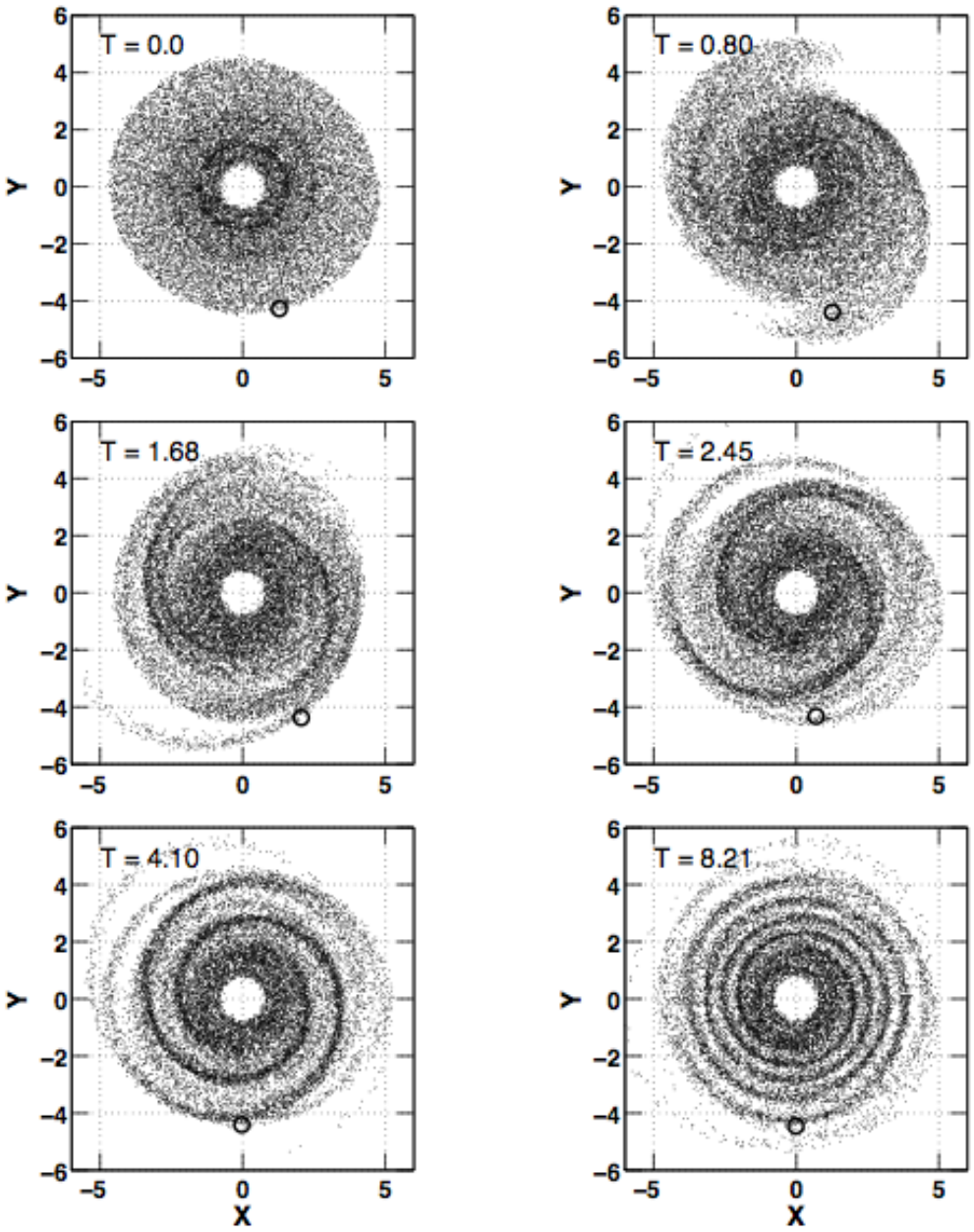

Figure 4.1 The numerical model at 6 times. The zero time in the first panel corresponds to the closest approach of the companion. Code time units are used as described in the text. The large circle marks the location of a particular outer disk particle. The second panel shows the disk about one outer disk rotation time after the encounter (270 Myr in the adopted scaling). The subsequent panels show the disk after about two, three, five, and ten outer disk rotation periods.

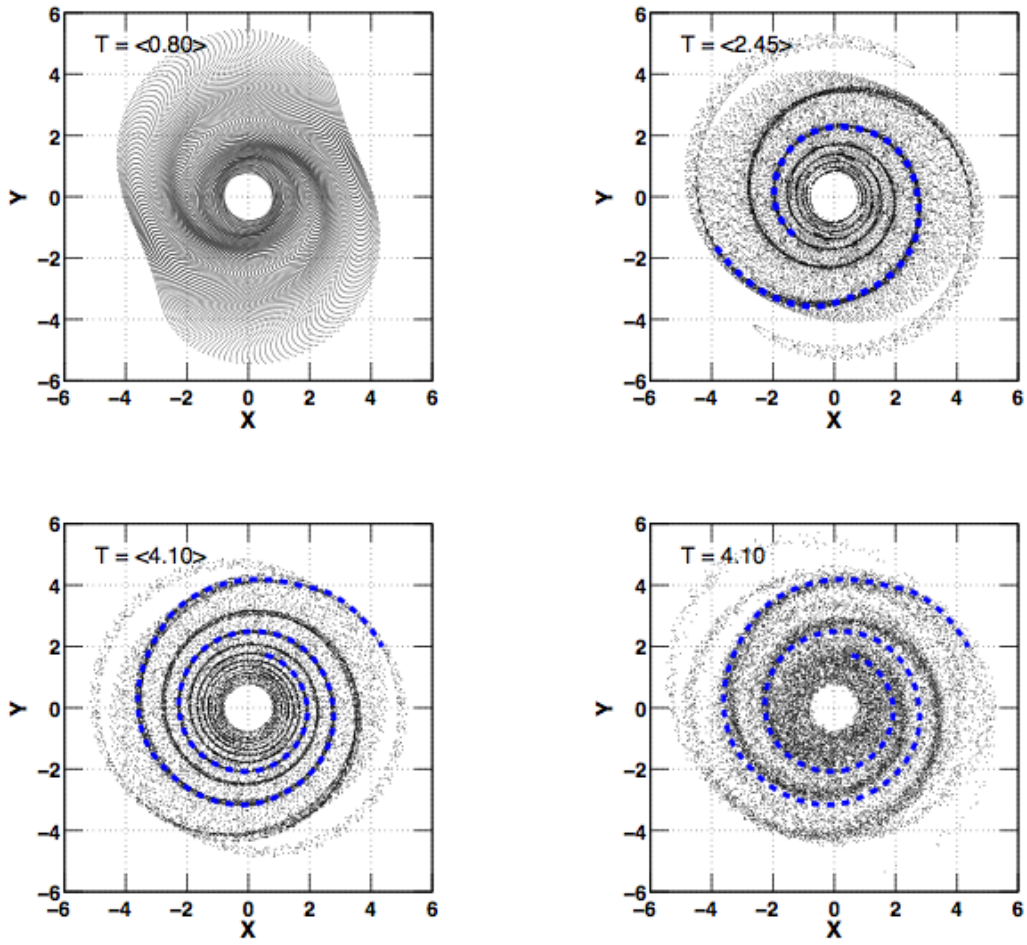

Figure 4.2 Analytic model evolution at three times is shown in the first three panels. The values in brackets indicate times after a constant time delay has been subtracted to allow better comparisons to the numerical model, as described in the text. The dashed (blue) curves in the last three panels show the analytic caustic center condition superimposed on one of the two symmetric spirals. The fourth panel shows the numerical model at the same time as the analytic model in the third panel. The caustic center curve, which is the same in both third and fourth panels, shows that analytic and numerical models are nearly identical in the outer disk, but differ in the inner disk, where the gravitational potentials are different.

4.4 Conclusions and ramifications

In summary, a surprising simulation result and its analytic representation provide new insights into the theory of weakly triggered spirals, and the longevity of tightly wrapped spirals. The classical theory of density waves would lead us to expect that weak triggering in a disk with a high value of Q would not produce strong waves. It would also predict the rapid dissipation of (kinematic) waves as they shear and wind up. The density enhancement in radial caustic zones overcomes these difficulties.

Tight spirals are reasonably well represented in catalogs of nearby galaxies, so they are evidently not too rare. NGC 488 is a prototypical example from the Hubble Atlas (Sandage 1961). The fact that these spirals take a number of typical rotation times to wind up (while maintaining a substantial density contrast) suggests that in most cases the companion will travel to large distances by the time the form becomes tightly wound. Thus, it is not expected that most tightly wound spirals produced by this mechanism to have obvious close companions. In a group or cluster environment it may be hard to identify the collision partner.

In some cases the collision partner may not be a galaxy. A disk galaxy falling past a cluster core at, for example, 2000 km s^{-1} = (0.5 Mpc)/(250 Myr) may also experience a quasi-impulsive tidal perturbation from the cluster core as whole. This is in addition to fast galaxy-galaxy encounters likely to occur in the cluster. Similar considerations apply to galaxies falling into groups. The gravitational potential of the spiral waves generated by this mechanism will draw in gas locally, triggering star formation. This seems to be confirmed by the relatively modest-sized star forming knots observed in the waves of some nearby tightly-wound spirals. However, since the waves cover much of the disk, the integrated star formation could be signicantly increased by these waves. Since the waves are primarily a stellar phenomenon, it is expected to increase the star formation within the stellar disk, but to have little effect in outer, gas dominated regions of disks.

It is noted that once the waves evolve to become tightly wound they may be very difficult to see directly, except in very nearby galaxies. The reader may inspect the various images of NGC 488 in the NASA Extragalactic Database. Many of them do not show the delicate wave

structure visible in the HST image. It is suspect that because this effect may be easy to induce in disk galaxies falling into larger structures, it plays a signicant role in galaxy harassment and in causing the Butcher-Oemler effect. However, there is little direct evidence for it in observations of Butcher-Oemler clusters (Butcher & Oemler 1978, but see Yamauchi & Goto 2004 where some of the blue, "passive" cluster galaxies may be tight spirals), nor in the Moore et al. (1996) harassment simulations. In the former case it is very likely that the tightly wound waves could not be resolved. The numerical resolution may also be a factor in the latter case. A number of the examples shown in the Moore et al. paper involved strong interactions, rather than the mild ones considered here. Moreover, harassment involves multiple interactions, whose effects have not been studied in the context of slowly breaking waves.

The mechanism described in this chapter does not apply to strongly self-gravitating spirals, nor those driven by large-amplitude global disturbances, like bars. The prediction that it operates in low-Q disks can be observationally checked. The mechanism is not applicable to young, gas-rich disks. In the general context of disk evolution it is more likely an agent of refinement. Nonetheless, it is reemphasized that it generates a class of nonlinear spirals whose structure and evolution are completely specified by a simple first-principles theory. For example, pattern speed and wind-up can be calculated straightforwardly given the structure of the potential (e.g., the unperturbed rotation curve).

Because the inputs of this theory are so simple it is also suspected that the waves may occur in other circumstances, and the theory may prove useful in applications beyond galaxy disks. Externally disturbed planetesimal accretion disks or Kuiper Belts might be possible areas of application. Even within the study of galaxy disks it should be a useful tool in addressing a variety of problems.

CHAPTER 5. SUMMARY AND FUTURE DIRECTIONS

5.1 Summary

The modeling work performed for the compact galaxy group, Stephan's Quintet (SQ), is the first numerical hydrodynamical study dedicated to the system which includes gas dynamical effects in the simulations. The major large-scale features of the system, such as the extended tidal features and the remarkable group-wide shock, enabled me to constrain the models reasonably well from the relatively close past to near future, while trying to reproduce multiple features of SQ. It has been found that with a sequence of two-at-a-time collisions, most of the major morphological and kinematical features of the group were well reproduced in the (best) models. The origins of the two parallel tails in SQ have been argued for long among several plausible formation hypotheses all based on observations. The SPH models suggest both tails may be formed simultaneously from a strong collisional encounter of NGC 7320c with NGC 7319, resulting in a thinner and denser inner tail than the outer one as observed. This is because the models showed that generating two substantial tails in a model one after one out of the same disk from two separate encounters, preserving the early generated tail at the later encounter while pulling another massive tail, was very difficult and unlikely. The model results also support the idea that the group-wide shock and the extra-nucleus starburst region SQ-A would be influenced by hydrodynamical effects from the high-speed collision between NGC 7318b and the IGM.

The numerical simulations of the interacting pair Arp 285 (NGC 2856/4) were intended primarily to study the origin of the peculiar tail-like feature that is perpendicular to the disk of NGC 2856, containing a series of star-forming complexes ("beads on the string"). Several conceptual ideas of the formation were tested in the models and proposed the probable

formation scenario of the feature from the model results, as material that has recently fallen out of a connecting bridge, swung around the galaxy that piled upon the north side. The model results were also used to interpret the recent multi-wavelength observations of the system by detailed comparison.

Fast collisions involving a disk with a high value of the Toomre Q parameter were modeled numerically and slowly developing spiral waves were discovered. The waves generated in the numerical models did not dissipate in a few orbital times; they persisted for a surprisingly longer time (more than 10 outer orbital period) becoming tighter. The numerical model results were compared to those of an analytic model, based on an impulse approximation with epicyclic orbits, and showed great agreement confirming the waves generated in the numerical models are kinematic waves not numerical artifacts. The simulation results would help to better understand the mechanisms of delicate spirals, and the longevity of tight spirals detected in nearby systems.

5.2 Future directions

It has been already obvious that most galaxies have interaction histories and interactions and mergers are one of the key drivers of galaxy evolution. To study the vast variety of interaction phenomena spanning huge spacial and time scales, numerical modeling has become an important and necessary mean, as it allows direct experiments and analyses via simulated media. I believe that the numerical studies of the three different interacting systems presented in this dissertation not only provide more information to investigate the dynamical evolution of the specific systems but also contribute to better understand the overall galaxy evolution in a bigger picture. The simulations of the widely separated interacting pair Arp 285, examining star-formation in the pile-up region, can be applied to the studies of the formation of tidal dwarf galaxies or globular clusters. The specific modeling work on the complex Stephan's Quintet system shows that multiple encounters in groups can be represented by two-at-a-time collisions. This would be extended to the various studies of higher redshift galaxy phenomena and general galaxy formation and evolution. The work on slowly breaking spiral waves by fast

collisions sheds light on spiral wave dynamics.

APPENDIX A. THE COMPUTATIONAL METHOD OF SMOOTHED PARTICLE HYDRODYNAMICS

The simulation code used in this research is the SPH code of Struck (1997). Here I explain the fundamentals of the SPH method and the smoothing kernel used in the code.

SPH is a Lagrangian (particle-based) method for simulating fluid flows. It was invented by Luicy (1977) and Gingold and Monaghan (1977) and has been reviewed by e.g. Monaghan (1992). Because SPH is Lagrangian, which does not require a grid or a mesh to compute spatial derivatives, it overcomes the limitations of typical grid-based methods on spatial resolution or global geometry. So SPH is efficient and suitable computational technique to model highly dynamic systems with arbitrary geometries, such as interacting galaxy systems, that are dominated by large-scale features.

In SPH, the fluid is divided into a set of N discrete fluid elements or particles, assuming the particle mass density is proportional to the fluid mass density. These particles have a non-zero spatial distance, so called smoothing length, which determines the resolution. Because the fluid is represented by a finite number of particles, the properties of the particles are locally averaged, using an appropriate interpolating kernel function, over volumes specified by the smoothing length in order to smooth out local statistical fluctuations in the particle number. Then, the average value of a physical field $f(\vec{r})$ can be determined by convolution with the kernel such that

$$< f(\vec{r}) > \equiv \int W(\vec{r} - \vec{r}', h) f(\vec{r}') d\vec{r}', \tag{A.1}$$

where W is the smoothing kernel, h is the smoothing length, and the integral is over all space. The smoothing kernel should satisfy the following two conditions:

$$\int W(\vec{r} - \vec{r}', h) d\vec{r}' = 1 \tag{A.2}$$

and

$$\lim_{h\to 0} W(\vec{r}-\vec{r}',h) = \delta(\vec{r}-\vec{r}')d\vec{r}'. \tag{A.3}$$

For numerical work, in which the values of $f(\vec{r})$ are known only at N finite number of points, the equation (A.1) can be approximated as

$$< f(\vec{r}) >= \sum_{j=1}^{N} m_j \frac{f_j}{\rho_j} W(\vec{r}-\vec{r}_j,h), \tag{A.4}$$

where the summation index j denotes a particle label; m_j and $\vec{r}_j$ are the mass and the position of particle j; ρ_j is the density associated with particle j; f_j denotes the value of f at $\vec{r}_j$. For example, the density at particle i can be expressed as

$$< \rho_i >=< \rho(\vec{r}_i) >= \sum_{j=1}^{N} m_j W(\vec{r}_i-\vec{r}_j,h). \tag{A.5}$$

As an important property of the SPH method, the spatial derivative of a quantity can be obtained (by using integration by parts and ignoring surface term) as

$$< \nabla f(\vec{r}) >= \sum_{j=1}^{N} m_j \frac{f_j}{\rho_j} \nabla W(\vec{r}-\vec{r}_j,h), \tag{A.6}$$

where the smoothing kernel W must be differentiable to at least the same order of any term in the dynamical equations.

The smoothing kernel adopted in the SPH code is the spherically symmetric spline kernel suggested by Monaghan & Lattanzio (1985) and corrected by Hernquist & Katz (1989):

$$W(r,h) = \frac{1}{\pi h^3} \begin{cases} 1-\frac{3}{2}\left(\frac{r}{h}\right)^2+\frac{3}{4}\left(\frac{r}{h}\right)^3, & 0 \le \frac{r}{h} \le 1, \\ \frac{1}{4}\left(2-\frac{r}{h}\right)^3, & 1 \le \frac{r}{h} \le 2, \\ 0, & \frac{r}{h} > 2. \end{cases} \tag{A.7}$$

The spherical symmetry of the kernel is required regarding gravitational field calculation and the linear and angular momentum conservations of the pressure forces. This spline kernel has continuous first and second derivatives. Using the spline kernel, the average value of a physical quantity at a given position depends on the quantities of the particles within a distance $2h$ from the position.

BIBLIOGRAPHY

Abazajian, K., et al. 2003, AJ, 126, 2081

Abraham, R. G., & van den Bergh, S. 2001, Science, 293, 1273

Allen, R. J., & Hartsuiker, J. W. 1972, Nature, 239, 324

Appleton, P. N., & Struck-Marcell, C. 1996, Fundamentals of Cosmic Physics, 16, 111

Appleton, P. N., Xu, K. C., Reach, W., Dopita, M. A., Gao, Y., Lu, N., Popescu, C. C., Sulentic, J. W., Tuffs, R. J., & Yun, M. S. 2006, ApJ, 639, L51

Arp, H. 1966, Atlas of Peculiar Galaxies (Pasadena: Caltech)

Barnes, J. E., & Hernquist, L. 1992, Nature, 360, 715

Barnes, J. E., & Hernquist, L. 1996, ApJ, 471, 115

Binney, J., & Tremaine, S. 2008, Galactic Dynamics (2nd ed.; Princeton, NJ: Princetion University Press)

Burbidge, E. M., & Burbidge, G. R. 1961, ApJ, 134, 244

Bushouse, H. A., Lamb, S. A., & Werner, M. W. 1988, ApJ, 335, 74

Butcher, H., & Oemler, A. 1978, ApJ, 219, 18

Chakrabarti, S. 2008, arXiv0812.0821

Chen, C. & Wu, H. 2007, AJ, 133, 1710

Chengalur, J. N., Salpeter, E. E., & Terzian, Y. 1994, AJ, 107, 1984

Chengalur, J. N., Salpeter, E. E., & Terzian, Y. 1995, AJ, 110, 167

Cluver, M. E., Appleton, P. N., Boulanger, F., Guillard, P., Ogle, P., Duc, P.-A., Lu, N., Rasmussen, J., Reach, W. T., Smith, J. D., Tuffs, R., Xu, C. K., & Yun, M. S. 2010, ApJ, 710, 248

Cutri, R. M., et al. 2006, Explanatory Supplement to the 2MASS All Sky Release and Extended Mission Products, http://www.ipac.caltech.edu/2mass/

de Vaucouleurs, G., de Vaucouleurs, A., Corwin, H. G., Buta, R. J., Paturel, G., & Fouqu, P. 1991, Third Reference Catalogue of Bright Galaxies, Springer-Verlag, New York

Elmegreen, B. G. & Efremov, Y. N. 1996, ApJ, 466, 802

Elmegreen, D. M., Elmegreen, B. G., Kaufman, M., Sheth, K., Struck, C., Thomasson, M., & Brinks, E. 2006, ApJ, 642, 158

Elmegreen, B. G., Kaufman, M., & Thomasson, M. 1993, ApJ, 412, 90

Feldmeier, J. J. et al. 2002, ApJ, 575, 779

Gerber, R. A., & Lamb, S. A. 1994, ApJ, 431, 616

Hancock, M., Smith, B. J., Struck, C., Giroux, M. L., Appleton, P. N., Charmandaris, V., & Reach, W. T. 2007, AJ, 133, 676

Hickson, P. 1982, ApJ, 255, 382

Hickson, P. 1994, Atlas of Compact Groups of Galaxies, Gordon and Breach, Switzerland

Hickson, P., Kindl, E., & Auman, J. R. 1989, ApJS, 70, 687

Holmberg, E. 1941, ApJ, 94, 385

Holtzman, J. A., et al. 1992, AJ, 103, 691

Holtzman, J. A., et al. 1996, AJ, 112, 416

Hunsberger, S. D., Charlton, J. C., & Zaritsky, D. 1996, ApJ, 462, 50

Hwang, J.-S., Struck, C., Renaud, F., & Appleton, P. N. 2010, in preparation

Keel, W. C., Kennicutt, R. C., Jr., Hummel, E., & van der Hulst, J. M. 1985, AJ, 90, 708

Kennicutt, R. C., Jr., Roettiger, K. A., Keel, W. C., van der Hulst, J. M., & Hummel, E. 1987, AJ, 93, 1011.

Larson, R. B. & Tinsley, B. M. 1978, ApJ, 219, 46

Leitherer, C., et al. 1999, ApJS, 123, 3

Martin, D. C., et al. 2005, ApJ, 619, L1

Mihos, J. C. & Hernquist, L. 1994, ApJ, 427, 112

Moles, M., Márquez, I., & Sulentic, J. W. 1998, A&A, 334, 473

Moles, M., Sulentic, J. W., & Márquez, I. 1997, ApJ, 485, L69

Moore, B., Katz, N., Lake, G., Dressler, A. & Oemler, A. 1996, Nature, 379, 613

Morris, S. L., & van den Bergh, S. 1994, ApJ, 427, 696

Ostriker, J. P. & Peebles, P. J. E. 1973, ApJ, 186, 467

Quinn, P. J. 1984, ApJ, 279, 596

Renaud, F., Appleton, P. N., & Xu, C. K. 2010, in preparation

Reshetnikov, V., Bournaud, F., Combe, F., Faúndez-Abans, M., & de Oliveira-Abans, M. 2006, A&A, 446, 447

Sandage, A. 1961, The Hubble Atlas of Galaxies (Washington, DC: Carnegie Institution)

Sanders, D. B., Scoville, N. Z., Young, J. S., Soifer, B. T., Schloerb, F. P., Rice, W. L., & Danielson, G. E. 1986, ApJ, 305, L45

Sanders, D. B., Soifer, B. T., Elias, J. H., Madore, B. F., Matthews, K., Neugebauer, G., & Scoville, N. Z. 1988, ApJ, 325, 74

Sellwood, J. A. 2010, arXiv1001.5430

Shostak, G. S., Allen, R. J., & Sullivan, W. T., III. 1984, A&A, 139, 15

Smith, B. J., Kleinmann, S. G., Huchra, J. P., & Low, F. 1987, ApJ, 318, 161

Smith, B. J., Struck, C., Appleton, P. N., Charmandaris, V., Reach, W., & Eitter, J. J. 2005b, AJ, 130, 2117

Smith, B. J., Struck, C., Hancock, M., Appleton, P. N., Charmandaris, V., & Reach, W. 2007, AJ, 133, 791

Smith, B. J., Struck, C., Hancock, M., Giroux, M. L., Appleton, P. N., Charmandaris, V., Reach, W., Hurlock, S., & Hwang, J.-S. 2008, AJ, 135, 2406

Smith, B. J., Struck, C., & Nowak, M. A. 2005a, AJ, 129, 1350

Smith, B. J., Struck, C., & Pogge, R. W. 1997, ApJ, 483, 754

Soifer, B. T., Sanders, D. B., Madore, B. F., Neugebauer, G., Danielson, G. E., Elias, J. H., Lonsdale, C. J., & Rice, W. L. 1987, ApJ, 320, 238

Struck, C. 1997, ApJS, 113, 269

Struck, C. 1999, Phys. Rep., 321, 1

Struck, C. 2006, in Astrophysics Update 2, Ed. J. W. Mason (Chichester, UK: Springer Praxis), 115

Struck, C., Dobbs, C. L., & Hwang, J.-S. 2010, in preparation

Struck, C., Kaufman, M., Brinks, E., Thomasson, M., Elmegreen, B. G., & Elmegreen, D. M. 2005, MNRAS, 364, 69

Struck, C. & Smith, B. J. 2003, ApJ, 589, 157

Struck-Marcell, C. 1990, AJ, 99, 71

Struck-Marcell, C. & Tinsley, B. M. 1978, ApJ, 221, 562

Sulentic, J. W., Rosado, M., Dultzin-Hacyan, D., Verdes-Montenegro, L., Trinchieri, G., Xu, C., & Pietsch, W. 2001, AJ, 122, 2993

Sundelius, B., Thomasson, M., Valtonen, M., & Byrd, G. G. 1987, A&A, 174, 67

Teuben, P. 1995, in ASP Conf. Ser. 77, Astronomical Data Analysis Software and Systems IV, ed. R. A. Shaw, H. E. Payne, & J. J. E. Hayes (San Francisco:ASP), 398

Trinchieri, G., Sulentic, J., Breitschwerdt, D., & Pietsch, W. 2003, A&A, 401, 173

Trinchieri, G., Sulentic, J., Pietsch, W., & Breitschwerdt, D. 2003, A&A, 444, 697

Toomre, A. 1977, The Evolution of Galaxies and Stella Populations, ed. B. Tinsley, R. Larson, p. 401. New Haven: Yale Univ. Obs.

Toomre, A. 1978, in IAU Symp. 79, The Large-Scale Structure of the Universe, ed. M. S. Longair & J. Einasto (Dordrecht: Reidel), p. 109

Toomre, A. 1981, The Structure and Evolution of Normal Galaxies, Proc. Advanced Study Institute, Cambridge, England, 1980 August 3-15, ed. S. M. Fall & D. Lynden-Bell (Cambridge: Cambridge Univ. Press), 111

Toomre, A., & Toomre, J. 1972, ApJ, 178, 623

Wallin, J. F. & Struck-Marcell, C. 1988, AJ, 96, 1850

Werner, M. W., et al. 2004, ApJS, 154, 1

Williams, B. A., Yun, M. S., & Verdes-Montenegro, L. 2002, AJ, 123, 2417

Xu, C. K., Iglesias-Pàramo, J., Burgarella, D., Rich, R. M., Neff, S. G., Lauger, S., Barlow, T. A., Bianchi, L., Byun, Y.-I., Forster, K., Friedman, P. G., Heckman, T. M., Jelinsky, P. N., Lee, Y.-W., Madore, B. F., Malina, R. F., Martin, D. C., Milliard, B., Morrissey, P.,

Schiminovich, D., Siegmund, O. H. W., Small, T., Szalay, A. S., Welsh, B. Y., Wyder, T. K. 2005, ApJ, 619, L95

Xu, C. K., Lu, N., Condon, J. J., Dopita, M., & Tuffs, R. J. 2003, ApJ, 595, 665

Xu, C. K., Sulentic, J. W., & Tuffs, R. 1999, ApJ, 512, 178

Yamauchi, C., & Goto, T. 2004, MNRAS, 352, 815

Zhang, X. 1998, ApJ, 499, 93